CHALMERS
UNIVERSITY OF TECHNOLOGY

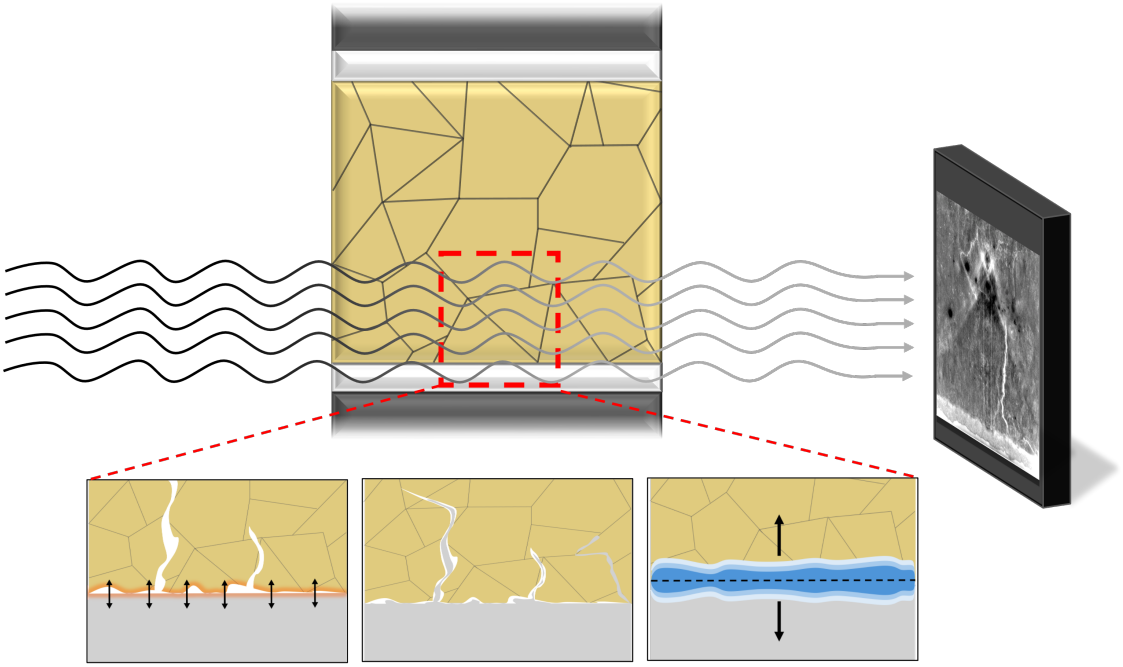

Investigating Degradation Mechanisms in Sodium Solid-State Batteries

A Study of Sodium Metal and Sulfide Solid Electrolyte Interactions using Electrochemical and X-ray Tomographic Characterization Methods

Master's Thesis in Physics

ANDREAS ERLANDSSON

DEPARTMENT OF PHYSICS
CHALMERS UNIVERSITY OF TECHNOLOGY
Gothenburg, Sweden 2025
www.chalmers.se

Master's thesis 2025

Investigating Degradation Mechanisms in Sodium Solid-State Batteries

A Study of Sodium Metal and Sulfide Solid Electrolyte Interactions using Electrochemical and X-ray Tomographic Characterization Methods

ANDREAS ERLANDSSON

CHALMERS
UNIVERSITY OF TECHNOLOGY

Department of Physics
Division of Materials Physics
Chalmers University of Technology
Gothenburg, Sweden 2025

Investigating Degradation Mechanisms in Sodium Solid-State Batteries
A Study of Sodium Metal and Sulfide Solid Electrolyte Interactions using Electrochemical and X-Ray Tomographic Characterization Methods
ANDREAS ERLANDSSON

Supervisor: Elin Dufvenius Esping, Department of Physics, Chalmers University of Technology
Examiner: Aleksandar Matic, Department of Physics, Chalmers University of Technology

Master's Thesis 2025
Department of Physics
Division of Materials Physics
Chalmers University of Technology
SE-412 96 Gothenburg
Telephone +46 31 772 1000

Cover: Schematic illustration of degradation mechanisms at the electrode-electrolyte interface, with an X-ray beam passing through the interface region and onto a detector.

Typeset in LaTeX
Printed by Chalmers Reproservice
Gothenburg, Sweden 2025

Investigating Degradation Mechanisms in Sodium Solid-State Batteries
A Study of Sodium Metal and Sulfide Solid Electrolyte Interactions using Electrochemical and X-ray Tomographic Characterization Methods
ANDREAS ERLANDSSON
Department of Physics
Chalmers University of Technology

Abstract

Solid-state sodium batteries are promising candidates for next-generation electrochemical energy storage, with improved sustainability and safety compared to current lithium-ion technologies. In addition, solid electrolytes could potentially enable the use of sodium metal anodes for increased energy density. However, these electrodes currently have short lifetime due to electro-chemo-mechanically coupled degradation mechanisms, which must be well understood in order to mitigate the problems and extend the lifetime of solid-state sodium batteries. This thesis investigates a sulfide solid electrolyte, with a particular focus on processes at the interface with sodium metal. The study involves electrochemical characterization techniques and imaging with X-ray tomographic microscopy, in order to gain insights into the processes that limit cell lifetime and efficiency. The results show rapid polarization of the cells, attributed to chemical degradation at the interface between sodium metal and the electrolyte. The resulting interphase layer fails to passivate the electrode, leading to capacity loss from the irreversible side reactions that continuously consume sodium metal and solid electrolyte. The use of chlorine-doped electrolytes and protective interlayers presents promising strategies to improve the interfacial stability and extend the lifetime of sodium metal electrodes.

Keywords: solid-state batteries, sodium metal anodes, sulfide electrolyte, X-ray tomographic microscopy, interphase characterization

Acknowledgements

First and foremost, I would like to express my deepest gratitude to my supervisor Elin Dufvenius Esping for the excellent guidance and support you have provided throughout this thesis project. You have been a great supervisor and it has been a pleasure working with you this spring! I want to thank my examiner Prof. Aleksandar Matic for welcoming me into his research group and for the valuable input and guidance during this work. A big thank you as well to Josef Rizell for showing me the ways of the lab and always taking the time to answer my questions - it has been great working with you! My sincere thanks extend to everyone at the Materials Physics division. Your kindness and welcoming attitude made me feel like a part of the team right away, it has been inspiring to write my thesis in the division thanks to you!

I would like to thank MAX IV and Anuj Prajapati, our local contact, for an excellent beamtime at the ForMAX beamline. Special thanks to Marita Afiandika for inviting me to join the beamtime and for allowing me to experience the fascinating world of synchrotron science for the first time.

Furthermore, I am thankful to ESRF and the European Battery Hub for the opportunity to visit the ID16B beamline for another exciting beamtime during my thesis work. I really appreciate the help from our local contact Gustavo Adolfo Pinzon Forero, Victor Vanpeene and the rest of the team at ID16B - it was a pleasure collaborating with you all!

I am grateful for the collaboration with the research group of Prof. Matteo Bianchini at the University of Bayreuth, and especially for the materials synthesis generously performed by Hao Guo.

Finally, I would like to thank my friends and family for their support and encouragement during my time as a Chalmers student!

Andreas Erlandsson, Gothenburg, June 2025

List of Acronyms

Below is the list of acronyms that have been used throughout this thesis listed in alphabetical order:

Current collector	CC
Computed tomography	CT
Coulometric titration time analysis	CTTA
Counter electrode	CE
Electrochemical impedance spectroscopy	EIS
Galvanostatic cycling with potential limitation	GCPL
Lithium-ion battery	LIB
Mixed-conducting interphase	MCI
Open circuit voltage	OCV
Polyether ether ketone	PEEK
Reference electrode	RE
Sodium-ion battery	SIB
Sodium solid-state battery	NaSSB
Solid electrolyte	SE
Solid-electrolyte interphase	SEI
Solid-state battery	SSB
Standard hydrogen electrode	SHE
Working electrode	WE
X-ray tomographic microscopy	XTM

Contents

1
Introduction

Rechargeable batteries are key components in the transition towards more sustainable energy sources, with applications such as electric vehicles and power grid storage. With an so-far unmatched combination of energy and power density, as well as long cycle life, lithium-ion batteries (LIBs) are currently dominating [1]. However, current LIBs are approaching their theoretical capacity limit while demands for even better performance and more sustainable technologies motivate the development of next-generation batteries [2].

Solid-state batteries (SSBs) have attracted significant research attention in recent years as a promising alternative to LIBs, potentially solving several of the issues seen in the current technologies. A major motivation behind the increased interest in solid electrolytes (SEs) is that they may enable the use of lithium metal anodes, or even anode-free architectures, leading to higher energy densities compared with conventional intercalation-type anodes such as graphite [3], [4]. Furthermore, replacing conventional liquid electrolytes with non-flammable solid-state electrolytes (SEs) could be a solution to some of the safety issues seen in LIBs.

Another important area of improvement is the sustainability of the batteries. The functions of multiple components in LIBs currently depend on scarce and expensive materials with problematic supply chains, in particular cobalt, but also lithium itself [5]. As sodium is more abundant than lithium, sodium-based battery technologies potentially enable cheaper batteries. In addition, many cathode materials for sodium-ion batteries (SIBs) are less dependent on cobalt, further improving the prospects of battery cost and sustainability [6].

While the potential benefits of sodium solid-state batteries (NaSSBs) indubitably seem plentiful, a number of key challenges remain to be addressed before they can be implemented commercially. One issue is the cycling stability of the cells, which relates to electro-chemo-mechanically coupled mechanisms occurring in the cell during cycling. A key area is the anode/SE interface where several key processes occur, including (i) (electro)chemical instability between SE and Na metal that causes Na consumption due to side reactions, (ii) mechanical failure, including crack formation and contact losses, induced by volume changes during plating and stripping of Na metal, and (iii) dendrite formation, which appears to be an issue for Na metal anodes, even with SEs [7]. The nature of these mechanisms needs to be well understood in order to mitigate the problems and extend the lifetime of NaSSBs.

The aim of this thesis project is to experimentally study NaSSBs, to gain a better understanding of materials and processes at the anode/electrolyte interface. More specifically, sulfide-based SEs and sodium metal electrodes are studied with focus on (i) investigating the interphase formation process by correlating results from electrochemical characterization methods and X-ray tomographic microscopy, (ii) identifying the interphase characteristics, including the evolution of impedance and morphology, (iii) correlating the interphase properties to the electrochemical performance and (iv) studying mechanical failure mechanisms and their connection to the interphase evolution.

2

Solid-State Batteries

The rechargeable battery is a type of electrochemical storage, where energy can be converted reversibly between chemical and electrical forms. In this chapter, the basic principles of rechargeable batteries are described, before introducing solid-state batteries and some key differences compared with current battery technologies. Anode materials for sodium batteries are described as well as some interfacial phenomena between the anode and the electrolyte, with focus on metallic anodes which are of particular interest in the context of solid-state batteries. Finally, some electrochemical characterization techniques are explained, which can be used to probe various properties of the battery and the materials within.

2.1 Fundamental Principles of Rechargeable Batteries

The fundamental structure in a battery is the electrochemical cell, consisting of two electrodes and an electrolyte. Energy is stored and released via redox reactions at the electrodes, a pair of chemical reactions where an atom or molecule gains (reduction) or loses (oxidation) electrons, changing the oxidation state of said atom or molecule. By convention, the positive electrode (cathode) and the negative electrode (anode) are the electrodes that are oxidized and reduced during discharge, respectively. During charging of the cell, the reversed reactions occur at the electrodes. The electrolyte conducts ions between the electrodes, while electrons are conducted via an external circuit. This is known as a "rocking-chair mechanism", as ions are shuttled back and forth between the electrodes during charge and discharge, see Figure 2.1. In this way, electrochemical cells can convert chemically stored energy to electrical energy and vice versa, and can thus be used as a power source in a variety of electrical applications. The electrolyte will be discussed in more detail in the next section, while the focus here will be on the electrodes.

The redox reactions are driven by a minimization of Gibbs free energy

$$\Delta G = -nFE_{\text{cell}}, \tag{2.1}$$

where n is the number of electrons involved in the reaction and $F = 96\,485\,\text{C/mol}$ is Faraday's constant. E_{cell} is the cell voltage, given by the potential difference between the electrodes as

$$E_{\text{cell}} = E_{\text{reduction}} - E_{\text{oxidation}}, \tag{2.2}$$

where $E_{\text{reduction}}$ and $E_{\text{oxidation}}$ are the potentials of the electrodes that are reduced and oxidised, respectively. The potential is a relative property, so a common reference must be used to determine the electrode potentials. For the standard (theoretical) potential, the reference $E^0 = 0\,\text{V}$ is chosen to be the reduction potential of hydrogen, i.e. the equilibrium potential of the reaction $2H^+ + 2e^- \rightleftharpoons H_2$, labelled the standard hydrogen electrode (SHE). The standard potential of other materials are then expressed relative to this reference, for example the standard potential of lithium is $-3.01\,\text{V}$ vs SHE and sodium $-2.71\,\text{V}$ vs SHE[8]. Similarly, the theoretical capacity is also a property of the active electrode materials that describe the amount of electrical charge that can be stored and released electrochemically, typically expressed in milli ampere-hours (mAh). The voltage and capacity are key properties of an electrochemical cell, as their product directly determines the amount of energy in watt-hours (Wh) that can be theoretically stored in the cell. Thus, it is desirable to have as high voltage and capacity as possible to maximize energy storage capabilities. The capacity of an electrode can be increased by having more active material, as it is an extensive property, so the specific capacity in mAh/g and specific energy in Wh/g are more interesting quantities to study when comparing electrode active materials.

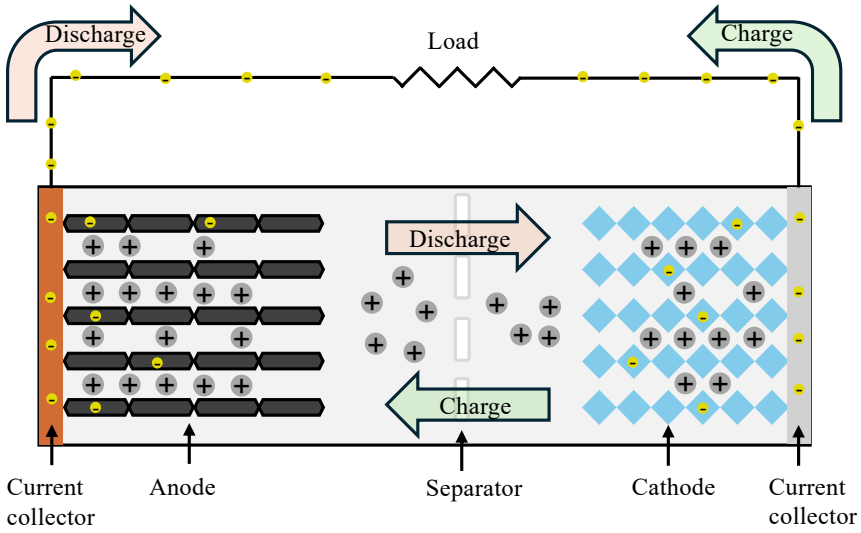

Figure 2.1: Schematic of the rocking chair mechanism, with the architecture of a conventional lithium-ion battery as an illustrative example.

While the theoretical voltage and capacity are the fundamental properties that determine the maximum energy that could possibly be stored in a battery, the actual energy storage available in practical batteries depend on many other parameters than purely the type of active materials. In practice, the electrode potentials will deviate from their theoretical equilibrium potentials, a phenomenon called polarization which is quantified in the overpotential $\eta = E - E_{\text{eq}}$[9]. Various polarization

effects within the cell cause losses where some of the theoretical energy is dissipated as heat, including ohmic polarization, activation polarization and concentration polarization, each contributing to the total polarization of the cell. Ohmic polarization, or IR drop, is a result of the total internal impedance in the cell, comprised of ionic resistance in the electrolyte and electronic resistance in the electrode active materials, current collectors and connections. Following from Ohm's law, the potential drop is proportional to the current drawn, hence the term IR drop. Activation polarization and concentration polarization both stem from the kinetics of the electrode reactions, where activation polarization relates to the electron-transfer kinetics in the redox reactions themselves. Meanwhile, concentration polarization is caused by limited mass-transfer kinetics of reactants and reaction products to and from the reaction sites at the electrode surface [8], [9].

An electrochemical cell with both cathode and anode active materials is called a "full cell", which is the standard configuration used in operational battery cells. However, it is common to study a specific electrode material and its interaction with the electrolyte. In these cases, rather than referring to the electrodes as anode and cathode, it is convenient to introduce the terms working electrode (WE), counter electrode (CE) and reference electrode (RE). The WE is the electrode of interest where one of the redox reactions occur, with the other half-reaction occurring at the CE. The potential of the WE is measured relative to the RE, ideally in a three-electrode setup where no current passes through the RE, ensuring a stable potential reference. In the practically simpler two-electrode configuration, the RE and CE are the same electrode, which prevents individual tracking of the WE potential as the potential of the CE can vary due to polarization effects when current is passed through the electrode [10].

2.2 Solid Electrolytes

The electrolyte is a critical component in the electrochemical cell by enabling the rocking-chair mechanism through ion transport between the electrodes, while also being electrically insulating to prevent internal short circuit. Thus, an electrolyte with high ionic conductivity, low electronic conductivity and good (electro-) chemical stability against the electrodes is important for high-performance, long-lasting batteries [7]. Conventional battery architectures have liquid electrolytes, as well as an electrically insulating separator layer to prevent internal electrical contact between the electrodes. In SSBs, the liquid electrolyte is replaced with a solid ion-conducting material. As the solid electrolyte also provides physical and electrical separation between the electrodes, there is no need for an additional separator as for electrochemical cells with liquid electrolytes. There are many classes of SEs, including inorganic ceramic compounds like sulfides, halides and oxides, as well as organic and inorganic polymer-based materials. Oxides have relatively high air and (electro)chemical stability, but requires expensive high-temperature sintering during fabrication. Halides are an emerging class of solid electrolytes (SEs) with good deformability and stability at high potential, suitable for cathode-electrolyte interfaces. However, they suffer from low ionic conductivity [7]. Polymer-based electrolytes ex-

ist both in the form of solid polymer matrix with sodium salts dissolved within, as well as intermediate solid-liquid gels. They typically have superior mechanical flexibility for easy processing and good interfacial compatibility, although their ionic conductivity is rather low compared with the other SE classes [11]. Sulfides have good ionic conductivity and deformability, but instead suffer from (electro)chemical instabilities. Since the primary electrolyte investigated in this project is a sulfide, the theory of sulfide SEs will be the focus in this section.

The ability of an ion to move in a solid electrolyte is called the mobility μ, whose relation to the ionic conductivity σ is described by an Arrhenius-like relation

$$\sigma = qn\mu \propto T^{-1}\mathrm{e}^{-E_\mathrm{a}/\mathrm{k_B}T}. \tag{2.3}$$

Here, q is the ion charge, n is the ion concentration, T is the temperature, E_a the characteristic activation energy for ion conduction and $\mathrm{k_B}$ is Boltzmann's constant [12]. The ion conduction mechanisms are different between crystalline and amorphous materials, although the main principle is the same. In solids, the atoms are bound into a rigid structure, either a crystalline structure or amorphous matrix, via electrostatic forces. Mobile ions, Na^+ in the case of SIBs or sodium metal batteries, need to overcome the electrostatic forces in order to migrate through the material, where chemical and/or electrochemical potential gradients can be the driving force to overcome this barrier [7]. There are three main conduction modes in crystalline electrolytes: vacancy diffusion, direct interstitial migration and concerted migration. Vacancy diffusion is simply the movement of an ion into a nearby stable vacancy site. Direct and concerted interstitial migration involves movement in between metastable interstitial sites, with and without the correlated displacement of any neighbouring ions, respectively. Amorphous electrolytes on the other hand are lacking when it comes to a unified theory of ion conduction, although a similar hopping theory is commonly used, as illustrated in Figure 2.2 [12].

2.2.1 Sulfide Solid-State Electrolytes

Sulfide-based Na-ion solid conductors belong to the category of inorganic SEs and have attracted research interest as electrolyte candidates for solid-state sodium batteries (NaSSBs). Compared with the oxide-based materials, who were the first materials to be considered for this application, sulfides possess several properties that make them promising as SEs. Electrostatic forces between sodium and sulfur are weaker compared with those between sodium and oxygen, because of the lower electronegativity of sulfur. Thus, Na-ion transport in sulfide-based materials is normally faster, resulting in higher ionic conductivity [13]. Furthermore, sulfides have good deformability and can be fabricated into pellets by cold-pressing at room temperature [7].

A sodium SSE that has received significant research attention is the ternary sodium tetrathiophosphate, Na_3PS_4 (NPS). NPS is a glass-ceramic, a class of inorganic materials which are partly crystalline [14]. It was first synthesized in 1992 through solid state reaction of sodium sulfide Na_2S and tetraphosphorousdecasulfide P_4S_{10},

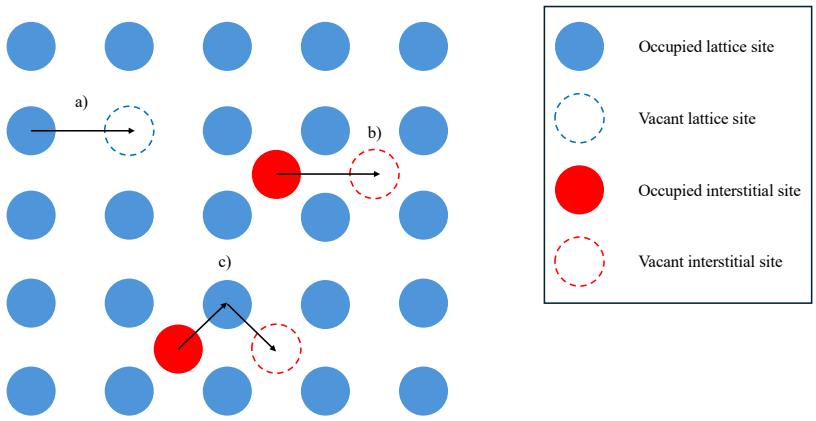

Figure 2.2: Illustration of three main ion conduction mechanisms in a crystalline materials. Ions can migrate a) directly to nearby lattice vacancy, b) directly from one interstitial site to a nearby one and c) concerted migration between interstitial and lattice sites via the simultaneous migration of an adjacent species.

a process where the precursors are heated to accelerate a chemical reaction. The resulting α-Na_3PS_4 had low ionic conductivity of only 4.17×10^{-3} mS/cm [15] at 50 °C. NPS was later synthesized from the precursors Na_2S and P_2S_5 by mechanical milling, resulting in a cubic crystal structure and a significantly higher ionic conductivity of 0.46 mS/cm at room temperature, sparking increased interest in NPS as a possible electrolyte for NaSSBs [16].

In addition to the good ionic conductivity, NPS has favourable mechanical properties. With a Young's modulus in the range of 7-14 GPa and shear modulus 3-5 GPa for cold-pressed pellets, NPS has good deformability. This can be compared with the NASICON-type solid electrolytes, belonging to the class of oxides, which have Young's moduli in the range of 50-100 GPa and shear modulus around 40 GPa [17], [18]. Low Young's and shear moduli have been proposed to be favourable in order to accommodate stress due to volume changes in the cell [12].

While the relatively high ionic conductivity and good mechanical properties are in favour for NPS as a viable sodium ion conductor for NaSSBs, concerns about the interfacial stability remain to be addressed. NPS, along with most sulfide-based electrolytes, are unstable against sodium metal. The upper and lower bounds of the electrochemical stability window of NPS vary slightly in literature, with $1.39 - 2.45$ V[19] and $0.9 - 2.5$ V[20] as some examples. The decomposition of NPS below the lower limit of the stability window is proposed to be

$$Na_3PS_4 + 8Na \rightarrow 4Na_2S + Na_3P, \tag{2.4}$$

based on X-ray photoelectron spectroscopy experiments [21], [22]. In spite of this apparent instability, there are contradictory reports that have both predicted good interfacial stability [23], as well as stable cycling performance when paired with sodium metal electrodes [24], highlighting the complexity of the interfacial processes

of between NPS and sodium metal which are not yet fully understood. Sodium metal electrodes will be elaborated on in Section 2.3.1, while interfacial phenomena in solid-state batteries will be discussed further in Section 2.4.

2.3 Anode Materials for Sodium Batteries

The choice of anode active material has major impact on the storage capabilities of rechargeable sodium-based batteries. Graphite, the most widely used anode material in LIBs, does not work for sodium systems. This is because the intercalation mechanism, where alkali-ions occupy sites in between the graphene layers of graphite, is not thermodynamically stable for sodium [25]. Thus, other materials have been explored to replace graphite, where non-graphitic carbon materials like hard carbon have been explored extensively as potential anode materials in SIBs. Sodium metal anodes could significantly increase the capacity compared to the intercalation-type materials typically used in conventional batteries, with its high theoretical capacity of 1165 mAh/g compared with theoretical estimates of 530 mAh/g for hard carbon [4], [26]. Another class of anode material is intermetallic anodes, based on alloying between sodium and other metals. The details of the latter two types of anodes will be discussed further in this section.

2.3.1 Sodium Metal Electrodes

The idea of alkali metal anodes dates back to the 1970s, when it was explored for lithium-based batteries with liquid eletrolytes [27]. However, safety issues relating to the fundamental process of lithium metal plating and stripping prevented widespread commercialization of lithium-metal batteries, leading to a temporarily reduced interest in the concept. Modern day demands for higher energy density batteries, in addition to advancements in battery materials and characterization techniques, have reignited research interests on the topic, which has also been adapted to sodium-based batteries. With their low standard potential of $-2.71\,\mathrm{V}$ (vs standard hydrogen electrode) and high theoretical specific capacity of 1165 mAh/g, sodium metal electrodes are highly interesting for next-generation batteries [28].

2.3.1.1 Anode-Free Cells

While electrodes with excess amounts of sodium metal can be useful in research to investigate various electrode and interface properties, there should ideally be no excess sodium metal in commercially viable batteries. There are several benefits to so-called anode-free (or reservoir-free) cells. Having no excess metal would maximise the energy density of the cell with respect to the anode active material. Additionally, anode-free cells do not require expensive handling of pure sodium metal for electrode fabrication, instead the electrode is formed *in situ* via electroplating, which will be described further below. Since there is no reservoir of sodium metal to replace lost sodium, it is critical to have full reversibility in the charge/discharge processes in anode-free cells, in order to have batteries with satisfactory lifetime. Reversibility

of the cycling processes is quantified by the Coulombic efficiency η_C given by

$$\eta_C = \frac{Q_{\text{discharge}}}{Q_{\text{charge}}} \tag{2.5}$$

where $Q_{\text{discharge}}$ and Q_{charge} are the amounts of charge transferred during discharging and charging of the cell, respectively. Thus, having less than 100 % Coulombic efficiency means that some charge is irreversibly lost due to some side reaction of other degradation mechanisms, which will limit the cell lifetime. Note that even seemingly high efficiencies of 99 % will lead to a cell lifetime (80 % of the initial capacity) of only 22 cycles, so very high efficiencies are required for commercially viable cells.

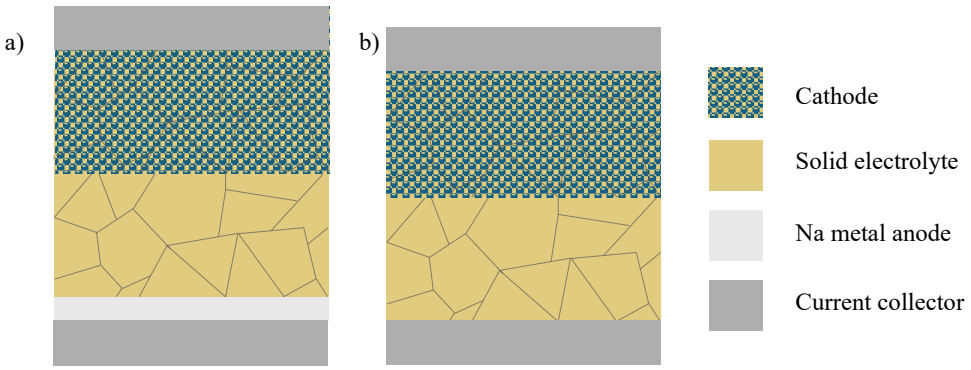

Figure 2.3: Schematic of a) a solid-state sodium metal battery and b) anode-free solid-state battery.

2.3.1.2 Electrochemical Plating of Sodium Metal

The mechanism for storing and extracting sodium ions in sodium metal electrodes differs significantly from conventional carbon-based electrodes. Instead of intercalating ions inside of a host structure, such as in between the graphene layers of graphite in LIBs, the ions are instead electrochemically plated and stripped on a substrate, without any surrounding host structure. The plating mechanism is closely related to the principles of nucleation and growth, in which the Gibbs free energy determines which is the thermodynamically preferable phase. When ions are deposited on the substrate, a nucleus will start to form. The difference in Gibbs free energy for the nucleus can be expressed as

$$\Delta G = \left(-\frac{4}{3}\pi r^3 \Delta G_{\text{V}} + 4\pi r^2 \gamma\right) f(\theta), \tag{2.6}$$

where r is the radius, ΔG_{V} is the Gibbs free energy change for homogeneous nucleation, γ is the surface energy between the electrolyte and the nucleus, and $f(\theta)$ an angle factor for the contact angle θ between the nucleus and the substrate, illustrated in Figure **??**. For small radii r, the positive contribution to ΔG from the surface term will be larger than the negative volume term, resulting in an overall positive ΔG, a thermodynamically unstable system. However, for radii above some critical radius $r > r_{\text{c}}$, there will be a net negative ΔG which makes further growth

of the nucleus thermodynamically favourable, so the formed nuclei will continue to grow spontaneously. The resulting electrochemical signature is therefore a voltage peak during plating, the nucleation overpotential, which is the potential required to form nuclei with radii $r > r_c$, illustrated in Figure 2.4b. Once such nuclei have formed, subsequent plating can occur at lower overpotential [29].

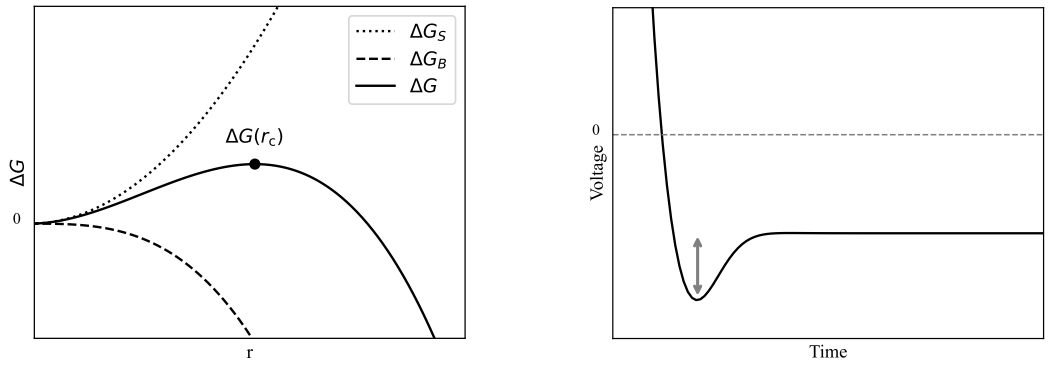

(a) **(b)**

Figure 2.4: a) Schematic illustration of Equation 2.6. The two terms $\Delta G_S \propto r^2$ and $\Delta G_B \propto -r^3$ correspond to the surface and bulk terms in the equation. For low $r < r_c$, the surface term will dominate, yielding a net increase in Gibbs free energy. Once the critical radius r_c is surpassed, the bulk term will dominate and subsequent growth of the nuclei results in a decrease in the total Gibbs free energy. b) Schematic voltage profile of the initial stages of sodium plating, where the highlighted voltage peak is a result of the energy barrier of nucleation.

2.3.2 Sodium-Tin Alloy Electrodes

Alloying sodium with other elements appears to have stabilizing effects on the otherwise highly reactive sodium metal, and so, various sodium alloys have been explored as anode materials [3]. Tin is a promising material for this purpose with its high specific capacity of up to 847 mAh/g. Furthermore, tin is inexpensive, abundant and nontoxic, making it a relatively safe material to work with which enhances its commercial viability [30]. At room temperature, seven equilibrium phases of Na-Sn alloy have been identified: $NaSn_6$, $NaSn_4$, $NaSn_3$, $NaSn_2$, Na_9Sn_4, Na_3Sn and $Na_{15}S_4$ [31]. However, more recent studies suggests that not all of these have been observed during the sodiation and desodiation of tin, highlighting that the sodiation mechanism of Na-Sn alloy is not yet fully understood [30]. Nevertheless, Na-Sn alloys show great promise as anode materials in NaSSBs [32].

2.4 Anode-Electrolyte Interfaces in Solid-State Batteries

The interface between the electrolyte and the anode is an important area of study, because of the complex processes occurring there, including side reactions between the anode and the electrolyte, the resulting growth of an interphase layer and subsequent volume changes, as well as contact loss and/or void formation due to the problematic nature of solid-solid interfaces. In this section, interfacial processes will be discussed, in particular those related to interfaces with sodium metal electrodes.

The solid-solid interfaces in NaSSBs allow for different phenomena compared to the solid-liquid interfaces in conventional batteries. Due to the ability to effectively transmit mechanical stress, solid-solid interfaces are susceptible to crack formation if the stress levels exceed the fracture threshold. While sulfides are considered to be relatively soft and ductile for a solid electrolyte, they are nevertheless brittle glass or glass-ceramics and prone to fracture, and fracture and crack growth becomes a serious issue to consider [12], [33]. The various (electro)chemical processes that occur at the interface can result in volumetric changes, as new phases are created as a product of reactions between the electrode and the electrolyte. Furthermore, volume changes at the interface occur due to plating and stripping of sodium metal during cycling, either through electrodeposition and depletion of the active electrode material, or unideally, through side reactions/interphase formation, resulting in electro-chemo-mechanically linked degradation at the interface [34].

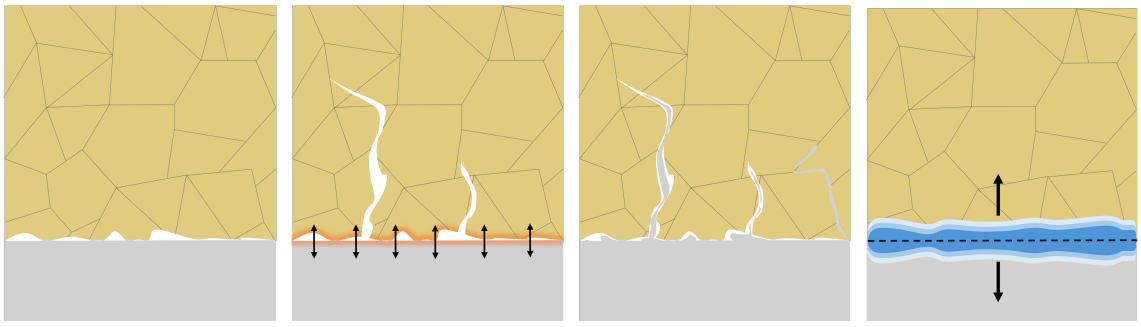

Figure 2.5: Various interfacial issues occurring and the anode-electrolyte interphase in solid-state batteries. a) Poor interfacial contact, leading to current constrictions at the narrow contact points. b) Mechanical strain/stress induced by volumetric changes, which can cause fracture in the electrolyte. c) Sodium metal dendrite and filament growth through cracks and along grain boundaries. d) Interphase formation as a result of (electro)chemical degradation. The interphase can either grow down into the sodium metal, up into the electrolyte, of both simultaneously.

Three classes of anode-electrolyte interfaces can be considered based on their thermodynamic and kinetic stabilities, illustrated in Figure 2.6. The first, and most

desirable, interface type is a thermodynamically stable interface. At these interfaces, the two phases in contact with each other do not react in any way as they are stable in their current state, so no interphase is formed through side reactions. The second type is a thermodynamically unstable interface, resulting in irreversible side reactions and the formation of an interphase layer. However, the interphase is ionically conducting and electronically insulating, which passivates the interface by preventing further side reactions from occurring. This type of interphase is sometimes referred to as solid-electrolyte interphase (SEI), due to its similar properties to the passivating interphases typically seen in lithium-ion batteries [27], [35]. The third interface type is also thermodynamically unstable, causing the formation of an interphase layer that is both ionically and electronically conducting, known as a mixed-conducting interphase (MCI). The mixed-conducting property promotes continuous side reactions in spite of the formation of an interphase layer between the electrode and the electrolyte. Most known SEs are thermodynamically unstable against sodium metal [7]. The next best scenario is the formation of an SEI, acting as a chemical separator layer to passivate the interface. Although there would be some initial capacity loss during the SEI formation, the passivating properties of the interphase could enable stable long-term cycling by preventing further degratdation between sodium metal and the electrolyte.

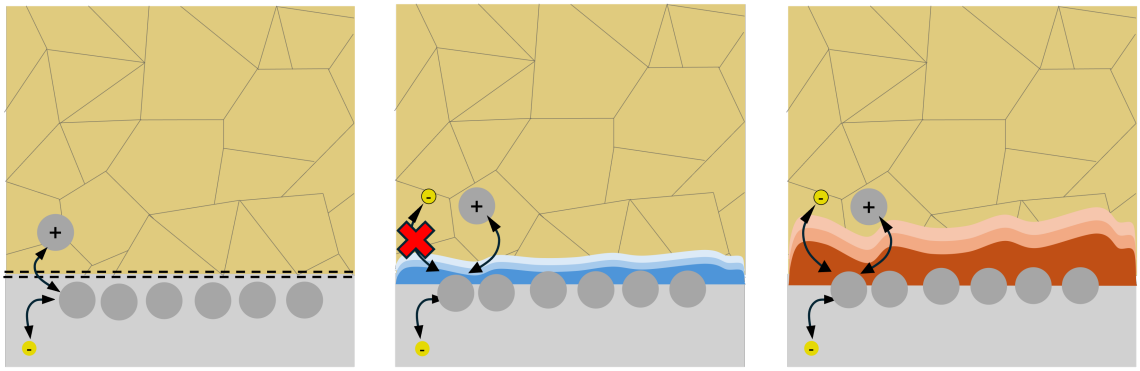

(a) **(b)** **(c)**

Figure 2.6: Illustrations of the three classes of anode-electrolyte interfaces. a) Thermodynamically stable interface between sodium metal and the SE. b) Passivating solid-electrolyte interphase (SEI) which is ionically conducting but electronically insulating. c) Unstable mixed-conducting interphase (MCI) which is both ionically and electronically conducting.

2.5 Electrochemical Characterization Methods

There are many electrochemical techniques that can be used to probe various properties of battery cells. This section introduces some common methods that have been used in this project.

2.5.1 Galvanostatic Cycling with Potential Limitation

Galvanostatic cycling with potential limitation (GCPL) is one of the most common electrochemical characterization protocols to study the performance of an electrochemical cell. The cell is cycled a pre-determined number of times, during which a constant current is drawn until the set potential limit is reached. Because of the constant current, the charge/discharge time is proportional to the amount of charge obtained. Cycling data from GCPL can be used to calculate the Coulombic efficiency of cells and, in combination with the other characterization methods performed in this project, assess chemical and morphological evolution at the anode/electrolyte interface. Note that Coulombic efficiency is not a relevant quantity for symmetric cells, that is, cells with sodium metal (or other sodium-ion reservoir) electrodes, because any lost sodium metal is replenished from the reservoir, preventing direct quantification of the amount of reversible capacity in the system.

2.5.2 Electrochemical Impedance Spectroscopy

Electrochemical impedance spectroscopy (EIS) is a common electrochemical characterization tool to characterize a variety of processes occurring in electrochemical cells. These processes can be complicated to study separately with time domain-based techniques such as CV and GCPL. However, by analysing the frequency domain when small perturbations are applied, the system can be approximated as linear and modelled as a transfer function. This is utilized in EIS, where the response of the system is measured after a small perturbation (sinusoidal voltage or current) is applied for a range of frequencies. This enables a separation of processes based on the time scales during which they occur [36]. Thus, EIS can be very useful for analysing interphase growth and other properties of the anode/electrolyte interface.

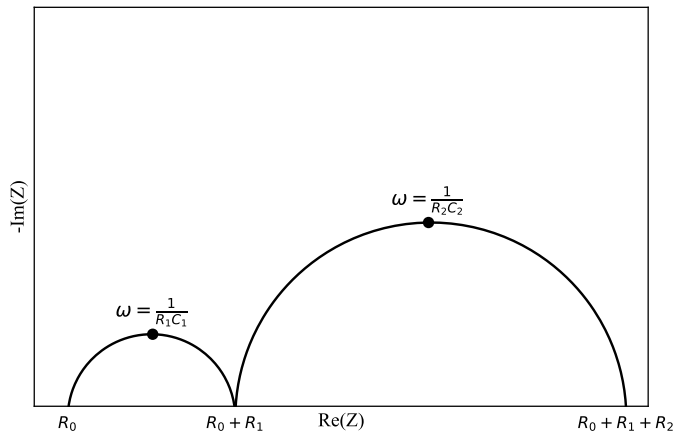

Figure 2.7: Schematic Nyquist plot for representation of EIS data with equivalent circuit modelling.

The impedance spectrum obtained from EIS contains a lot of information about

all parts of the system, which is not trivial to extract. Impedance contains both a real and imaginary part, corresponding to resistive and capacitive behaviour of the cell, respectively. Thus, it is convenient to represent EIS data in the form of a Nyquist plot, as illustrated in Figure 2.7. By modelling the various processes in the cell with an equivalent RC-circuit, the properties of each individual process can be quantified. However, this is a very idealized situation and much consideration of the complexity of an electrochemical cell needs to be taken into account before assigning equivalent circuit models to specific processes. Nevertheless, some general rules of thumb can be used to interpret EIS data in Nyquist plots for solid-state batteries. R_0 corresponds to the bulk Ohmic resistance of the electrolyte. The following semicircles are typically assigned to various interfacial processes, such as electrode-electrolyte interface impedance, charge-transfer impedance during the redox reactions and grain boundaries within the electrolyte. In these processes there is a capacitive contribution from the formation of electrochemical double layers at interfaces, as well as from the dynamics of mass-transfer of ions [36], [37].

2.5.3 Coulometric Titration Time Analysis

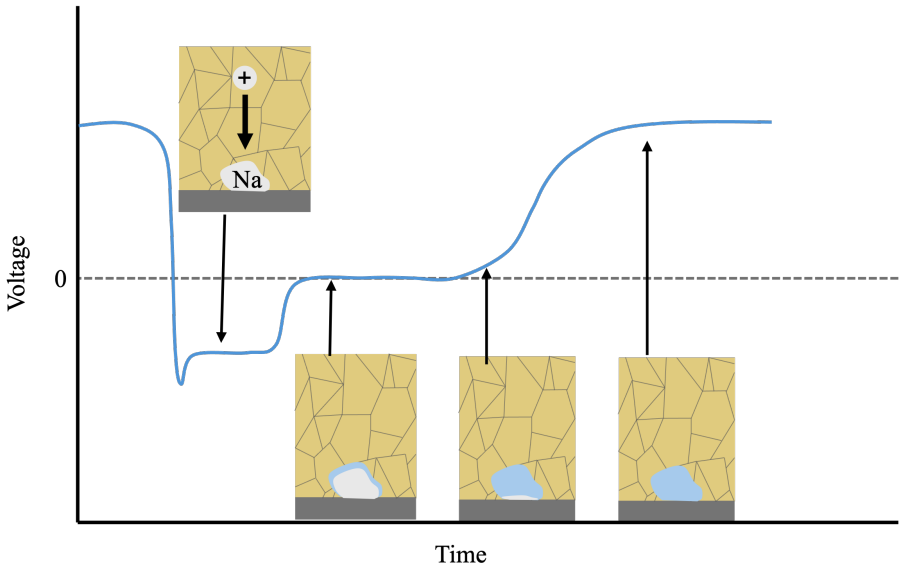

Figure 2.8: Schematic illustration of the main principles of coulometric titration time analysis. The cell voltage drops below 0 V during the deposition phase, during which some amount of sodium metal is plated onto the CC. The cell is then rested at OCV and the cell voltage remains at 0 V until the sodium metal gets consumed in side reactions, forming an interphase layer (highlighted in blue).

Coulometric titration time analysis (CTTA) is a relatively new characterization method to quantitatively investigate side reactions at the anode/SSE interface, introduced by Aktekin et al. in 2023 for lithium metal solid-state cells [38]. In CTTA, a small amount of metal is deposited on the current collector in an anode-free configuration (e.g., Al/NPS/Na). With Na deposited on the current collector, the cell effectively becomes symmetric and the cell voltage goes to 0 V vs Na/Na^+. In an

ideal cell with no side reactions or other mechanisms of Na metal degradation, the cell voltage would thus remain at 0 V indefinitely. However, in real cells with various interfacial instabilities, the deposited Na can eventually be completely consumed. During this process the cell voltage will eventually start to rise, at which point the time is recorded and a new cycle of Na deposition and open-circuit voltage (OCV) monitoring is initiated. OCV means that the cell voltage is measured when no current is flowing through the circuit, so no external load is connected to the cell. The procedure is then repeated and the time of the OCV period is recorded for each cycle, providing a basis for quantitative analysis of interphase passivation, rate of side reactions and other possible degradation mechanisms. The technique can also give some indications of the surface area of deposited Na metal. If the deposited Na forms dendritic structures rather than a homogeneous metal layer, the surface area will be higher and thus the rate of Na consumption via side reactions will be faster.

3

X-Ray Tomographic Microscopy

X-ray tomographic microscopy (XTM) is an imaging technique that can be used to probe the microstructure of battery materials, allowing for *in-situ* and *operando* 3D characterization. The fundamental technique used in XTM is the computed tomography (CT) scan, which was developed in the 1970s and awarded with the Nobel Prize in 1979, following the revolutionary impact it had on medical diagnostics [39]. While CT is commonly associated with its usage as a medical tool, its applications now span across many areas of science, including pharmaceutical research, materials science and life sciences [40]–[42].

3.1 Basic Principles of Computed Tomography

XTM exploits the interaction of X-rays with matter to produce contrast between the different phases present in the sample of interest. XTM can be performed using both lab-based and synchrotron X-ray sources. Synchrotrons are large-scale research facilities that have several benefits over lab-based systems, including high flux beams, easily tunable beam energies, and highly parallelized and coherent beams, which enables high-resolution imaging. X-rays, being electromagnetic radiation, interacts with a medium according to the mediums refractive index

$$n = 1 - \delta + i\beta, \tag{3.1}$$

where the real part δ and imaginary part β relate to the absorption and phase shift of X-rays, respectively [43]. Thus, there are two X-ray modulation mechanisms that can be utilized in XTM as contrast between different phases, namely attenuation and phase contrast. X-ray beams attenuate exponentially when passing through a medium, described by the Beer-Lambert law

$$I(d) = I_0 \mathrm{e}^{-\mu d}, \tag{3.2}$$

where I is the X-ray intensity measured at the detector, I_0 is the intensity of the initial beam, μ is the absorption coefficient and d is the thickness of the sample. Various forms of absorption and scattering contribute to the total attenuation, however the dominant mode is photoelectric absorption, which is described by the relation

$$\mu = \frac{\rho Z^4}{AE^3}, \tag{3.3}$$

where ρ is the density, Z is the atomic number, A is the atomic mass and E is the X-ray beam energy [44].

Utilizing the above, three-dimensional images can be reconstructed from two-dimensional projections by rotating the sample 180° and acquiring projections from a large number of different angles. The projection data is collected into so-called sinograms, line profiles containing the angular variation of X-ray transmission for each row of pixels. The sinograms can then be used to reconstruct a three-dimensional image through computational methods, where Filtered Back Projection is a common method [45]. The resulting 3D image consists of vertical and horizontal slices, which are arrays of voxels, the 3D equivalent of pixels. The greyscale intensity of each voxel corresponds to the amount of X-ray absorption, which can then be used to distinguish the various phases present in the sample [44].

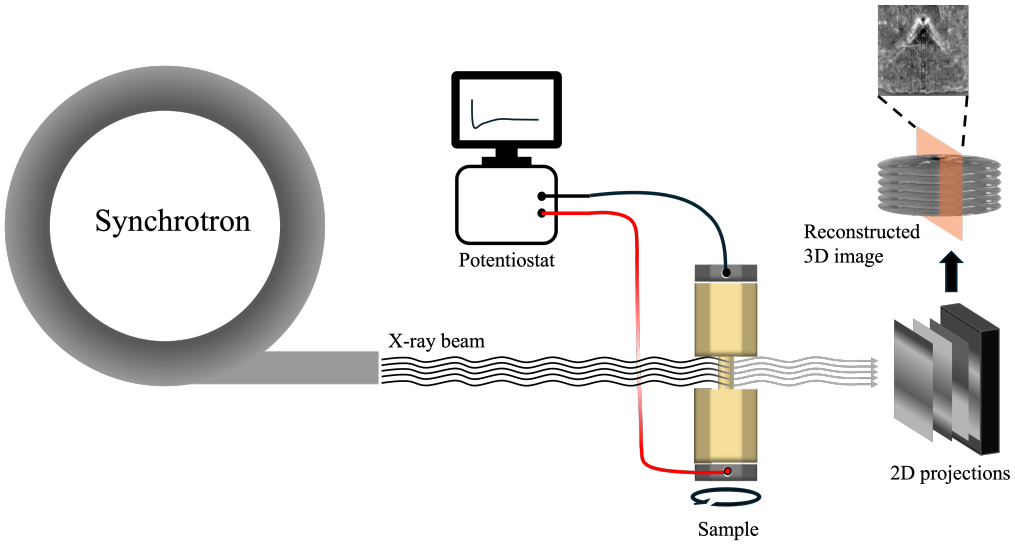

Figure 3.1: Schematic setup of a synchrotron X-ray tomography experiment.

Attenuation contrast alone may be insufficient to distinguish materials with similar attenuation coefficients, especially for elements with low atomic numbers. In those cases, phase contrast can be used in addition to attenuation contrast to enhance the differentiation between phases and improve image resolution. This is possible since the variation in δ, the real part of the refractive index in Equation 3.1 corresponding to the phase shift, is typically several orders of magnitude larger for lighter materials than the variations in β [46]. One technique to incorporate phase contrast into XTM is holotomography. The phase of electromagnetic radiation cannot be measured directly, however phase shifts can be detected indirectly based on its effect on the Fresnel diffraction pattern of the wavefront. It was discovered that the high coherence of synchrotron X-ray radiation could be utilized to retrieve phase information about the sample by scanning the sample at multiple distances from the detector and analysing the interference patterns at each distance. Along with a cone-shaped beam for enhanced magnification, this technique enables high-contrast 3D imaging with sub- 100 nm resolution [47]–[49].

3.2 Imaging Battery Materials with Computed Tomography

XTM has proven to be highly useful in battery research, having been deployed to study various effects in both liquid-electrolyte and solid-state systems [50], [51]. Some of the major benefits of the technique lie in the high resolution imaging, both spatially and temporally, allowing for effective *ex situ*, *in situ* and *operando* characterization. *Ex situ* measurements is the simplest mode of the three, where single scans are taken of the cell in some electrochemical state, not necessarily in a representative condition of a functional cell. For instance, the cell can be disassembled and the materials extracted from their operational environment which enables potentially simpler experimental setups. *In situ* involves scanning the same cell at different electrochemical states without disassembling the cell. Finally, *operando* experiments are real-time measurements of the cell during operation, such as during charge/discharge cycles of the cell [46]. *In situ* and *operando* measurements pose more demanding requirements on the experimental setup, since the cell configuration has to be suitable for both electrochemical and X-ray tomographic measurements simultaneously. Since XTM measurements are made in air, the cell has to be air tight to prevent exposure to oxygen and water. Furthermore, the cell configuration has to be very small to avoid excessive X-ray absorption through the sample, which would prevent effective imaging. Cell diameters on the order of 1-2 mm are suitable, which is significantly smaller than typical lab-scale cells on the order of 10 mm [44], [51], [52].The smaller diameter is something to consider when analysing electrochemical performance using tomography cell setups, as they may perform differently than larger cells.

In addition to having suitable measurement modes for studying batteries, XTM also has suitable spatial resolution and field of view to capture many features of interest. Particle size in sulfide-based electrolytes are typically on the order of a few micrometers, which is visible in both micro-tomography (microCT) and nano-tomography (nanoCT) with resolutions of 1.3 µm and 50 nm, respectively [53], [54]. Electrodeposition of sodium metal onto the current collector is a very interesting phenomenon to image *in situ*/*operando*. The thickness of a dense and homogeneously plated layer of sodium metal can be estimated as

$$\text{Thickness (µm)} = \frac{C \times M}{n \times \text{F} \times \rho} \times 3.6 \times 10^4, \tag{3.4}$$

where C is the plated (specific) capacity in mAh/g, M is the molar mass in g/mol, n is the number of electrons transferred by each reactant, $\text{F} = 96\,485$ C/mol is Faraday's constant, ρ is the density in g/cm^3 and 3.6×10^4 is a conversion factor going both from mAh/g to C/g and from cm to µm. Using $M = 22.9$ g/mol, $n = 1$ and $\rho = 0.97$ g/cm^3 for sodium metal[55], the thickness of a 1 mAh/cm^2 plated layer is estimated to be ~ 9 µm, which is also in a relevant length scale to capture with XTM.

In the context of cells based on the NPS solid electrolyte, as well as sodium metal and sodium-tin alloy electrodes, we could expect to find a number of elements and

compounds at the electrolyte/electrode interfaces. The linear attenuation coefficient of these elements and compounds at the beam energies of interest are collected in Table 3.1.

Table 3.1: Summary of the linear attenuation coefficient μ for the elements and compounds that are likely to be present at the electrolyte/electrode interface in NPS-based (symmetric and asymmetric) cells with sodium metal or tin alloy electrodes [56].

Element/compound	μ at 16 keV [cm^{-1}]	μ at 29.6 keV [cm^{-1}]
Na	3.4	0.8
Na_3PS_4	23.1	3.5
Al	15.7	3.0
Na_3Sn	61.4	69.4
Na_2S	12.5	2.4
Na_3P	9.1	1.8

4

Methods

This chapter describes the materials used and the procedures for the experiments performed in this project.

4.1 Cell Assembly

All electrochemical and X-ray characterization of cells in this project were, unless specified otherwise, done in a so-called tomography cell, see Figures 4.1 and 4.2. The setup is based on a polyether ether ketone (PEEK) cell housing. PEEK is a plastic with good chemical resistance and low X-ray absorption, making it suitable for XTM of highly reactive alkali metals and other chemically sensitive materials. The battery is assembled within the narrow waist of the cell, where the inner and outer diameters are 2 mm and 4 mm respectively. The sodium electrodes are mounted on stainless steel pins/screws which are inserted into the cell. Stack pressure is applied to the small top pin via a spring with known spring constant k and compression distance x, resulting in a controlled force F (and thereby pressure) applied to the cell as a result of Hooke's law

$$F = kx. \tag{4.1}$$

2 MPa stack pressure was used, unless noted otherwise. The ends of the cell house are sealed with rubber O-rings to prevent air from entering the cell.

NPS electrolyte and Na_3Sn powders were prepared by the group of Matteo Bianchini. Synthesis procedures and materials characterization is included in Appendix A. Electrolyte pellets were prepared by pressing 5 mg of the NPS powder in a 1.85 mm diameter die set for three minutes, using the equipment shown in Figure 4.3. The pressure was applied with a torque wrench, where 1.2 Nm, 3 Nm and 4 Nm were used, corresponding to 120 MPa, 310 MPa and 410 MPa, respectively. For asymmetric cells with Na_3Sn as CE, the two powders were pressed sequentially on top of each other to form a single pellet. First, 5 mg NPS was pressed for 3 min at 120 MPa. Then, 5 mg Na_3Sn was placed into the same die set and the stack was pressed for 3 min at 410 MPa.

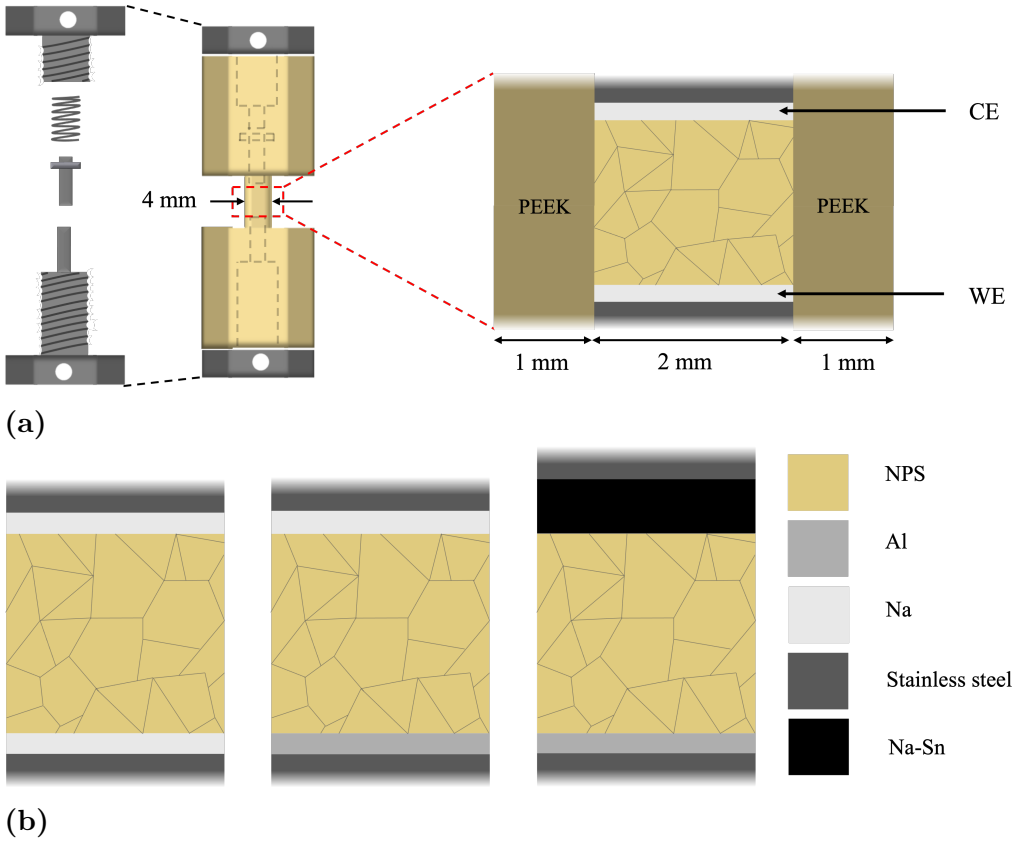

Figure 4.1: Schematic illustration of the cell setup used in the experiments. a) Overview of the PEEK cell house, which has a narrow waist where the cell is located, with a 4 mm and 2 mm outer and inner diameter, respectively. The stainless steel components used to enclose the cell are shown to the left the assembled cell, comprising top and bottom pins and a spring to apply stack pressure onto the top pin. A cross section of the cell is highlighted to the right, with a symmetric Na/NPS/Na configuration as example. The orientation of the cell was such that the working electrode (WE) and counter electrode (CE) are the bottom and top electrodes, respectively. b) The cell configurations that were tested (from left to right): symmetric Na/NPS/Na, asymmetric Al/NPS/Na and asymmetric Al/NPS/Na-Sn.

Figure 4.2: The tomography cell parts, comprising (from top to bottom), stainless steel top screw, spring, stainless steel top pin, PEEK cell house and two variants of the stainless steel bottom pin/screw. The variant to the right has an extension pin at the bottom, which was used for easier alignment during the nanoCT experiment. The two O-rings can be seen to the right, which are inserted between the steel screws and the PEEK cell to seal the cell house air-tight.

Sodium metal electrodes were prepared from a sodium dry stick (Thermo Scientific). A fresh piece of sodium was cut out from the stick by removing the outer edges with a scalpel. The resulting piece of sodium was put in between sheets of Celgard (2400) separator and rolled to a 300 µm foil using a hand-operated calender machine (WCHO-6080G, Wellcos Corporation). 1 mm ⌀electrodes were then punched out from the foil using a Miltex biopsy punch with 1 mm plunger. The symmetric Na/NPS/Na cell that was built and measured at ESRF is an exception to this procedure, where instead sodium electrodes were prepared from sodium cubes in mineral oil (Sigma-Aldrich). The outer surface of the cube was wiped clean from oil and a fresh piece of sodium was cut out from the middle of the cube, which was then rolled to a foil in between Celgard sheets.

One lithium-based cell was built and tested in this project, using the sulfide-based electrolyte Li_6PS_5Cl (LPSC, NEI Corporation, fine powder 1 µm). The electrolyte pellet was fabricated according to the same procedure as NPS, with a fabrication pressure of 310 MPa for 3 min. The cell architecture was a symmetric Li/LPSC/Li with 1 mm ⌀Li electrodes punched out from 300 µm thick foil (Honjo Metal).

All cell assembly and characterization, except for XTM, was performed in an argon-filled glovebox to minimize air and humidity contact. For XTM, the cells were first built in the glovebox as previously described, and taken out of the glovebox to the beamline once the cell house has been sealed air tight with the O-rings. Data showing the sealing properties of the cell housing is presented in Appendix B.

(a)

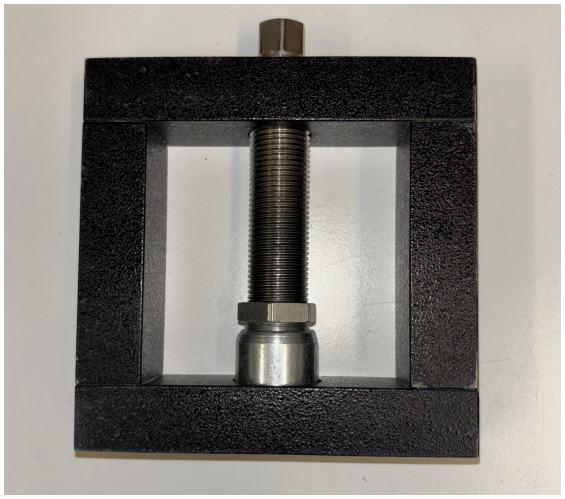

(b)

(c)

Figure 4.3: Equipment used for pressing electrolyte pellets, comprising a) 1.85 mm die set consisting of a bottom piece (left), top piece (right) and a plunger (bottom), b) the manual hand pressing rig that the die set was inserted into and c) the torque wrench used to apply a controlled amount of pressure on the press rig.

(a)

(b)

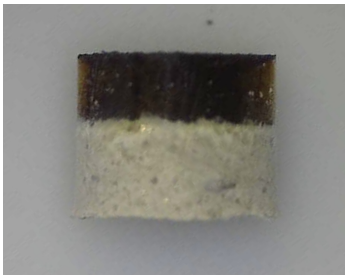

(c)

Figure 4.4: Microscope images of the fabricated pellets, a) NPS , b) Na_3Sn and c) stacked NPS/Na_3Sn (yellor/black) seen from the side.

4.2 Electrochemical Characterization

All electrochemical characterization was performed using a multichannel potentiostat (BioLogic VMP-300). Cell assembly was done such that the working electrode was on the bottom pin, away from the spring, connected to the positive pole. Thus, plating of sodium on the working electrode corresponds to a negative potential.

GCPL measurements were performed using a current density of 7.85 µA, unless specified otherwise, corresponding to 1 mA/cm^2 for the 1 mm Na electrodes. The cut-off voltage limit was set to ±2 V.

EIS was measured in the frequency interval 1 MHz − 100 mHz with ten points per decade. The excitation voltage was 10 mV.

CTTA was performed in a slightly modified way compared with the procedure presented by Aktekin et al. [38]. 0.44 mA/cm^2 was deposited on the Al CC for 1 h in an asymmetric Al/NPS/Na_3Sn cell. The cell was then rested at OCV and the potential was monitored for 3 h.

4.3 X-ray Tomographic Microscopy

This section describes the two different synchrotron X-ray tomography experiments that were carried out in this project.

4.3.1 Microtomography

X-ray microtomography (microCT) was performed at the ForMAX beamline at MAX IV [53]. The experiment was done with a monochromatic parallel beam with a beam energy of 16 keV. A 10X magnification objective was used, resulting in a vertical and horizontal image size of 1012 µm and 650 µm, respectively. 1800 projections were taken for each scan, equally distributed along a 180° rotation of the samples. Only attenuation contrast was used for this experiment, and the reconstructions were made on the MAX IV HPC cluster using the `TomoPy` toolbox [57].

Three *ex situ* samples were prepared and cycled in a argon-filled glovebox at Materials Physics' battery laboratory and brought to the beamline in Lund in air tight pouches: Al/NPS/Ns_3Sn asymmetric cell, Al/NPS/Na asymmetric cell and Na/NPS/Na symmetric cell. The Al/NPS/Na_3Sn cell had a 3 h 7.85 µA deposition on the Al CC. The NPS pellet was pressed for 30 min at 120 MPa, after which the Na_3Sn powder was added on top and the stack was pressed for 30 min at 120 MPa again, for a total of 1 h pressing time of the NPS. The Al/NPS/Na half cell had 7.85 µA deposited onto the Al CC for approximately 1h, with a NPS pellet pressed at 310 MPa for 3 min. Finally, the symmetric Na/NPS/Na cell was fabricated using 120 MPa for 1 h, without any cycling.

4.3.2 Nanotomography

Nanotomography (nanoCT) was performed at the ID16B beamline at ESRF [54]. The beam energy was 29.55 keV with a cone-shaped (pink) beam whose minimal size at the nearest measurement location closest to the focal point is 50 nm. Two different scan modes were used. First, the so-called "fasttomo" (nano-FT) meaning a single-distance tomogram with the sample at the 250 nm position. Secondly, the nano-holotomography (nano-HT) mode where one tomogram taken at four different distances, from the 50 nm position to the 250 nm position. The detector size was 2048×2048 pixels, resulting in $102.4 \times 102.4\,\mu m^2$ and $512 \times 512\,\mu m^2$ field of view for 50 nm and 250 nm voxel size, respectively.

Two samples were measured: an asymmetric Al/NPS/Na_3Sn cell and a symmetric Na/NPS/Na, both cells built on site in the electrochemistry lab at ESRF. The asymmetric cell was used for an *in situ* titration measurement, with the procedure as follows. A FT image was taken of the pristine cell. The cell was then set to $1\,mA/cm^2$ deposition on the Al CC for 2 h 20 min with FT images taken every 20th minute. The deposition was paused and the cell was set to OCV during each image acquisition. After deposition, the cell was set to OCV for 1 h, once again with FT images taken every 20th minute.

The symmetric Na/NPS/Na cell was imaged *in situ* with FT taken 2 h after the cell was built, having rested at OCV up until then. The cell was then taken out of the beam and was put aside to rest at OCV again. Another FT image was taken of the cell 18 h after it was built, along with a HT scan.

5
Results and Discussion

In this chapter the results from the project are presented and discussed. First, GCPL data on symmetric and asymmetric cells with Na metal electrodes are shown. Moreover, the cycling data is accompanied with EIS measurements that highlight possible mechanisms that influence the cycling performance. Following these results, Na metal counter electrodes are replaced with Na_3Sn alloy and comparisons are made between the two setups. In addition to GCPL, CTTA data are presented to further highlight interfacial effects. Finally, XTM images are presented for visual information of chemo-mechanical effects correlated to the electrochemical data.

5.1 Electrochemical Performance

As a first step to investigate the NPS electrolyte and its interaction with sodium metal electrodes, GCPL measurements were performed. This section presents and discusses results on galvanostatic cycling of both symmetric and asymmetric cells. Additionally, a comparison is made between sodium and lithium-based SSBs in symmetric cell configuration.

5.1.1 Galvanostatic Cycling of Symmetric Cells

Figure 5.1 shows the cycling performance of symmetric cells using two different areal capacities, $1\,mAh/cm^2$ and $3\,mAh/cm^2$. Right away, one can notice the rather large overpotential at the initial stages of cycling, around $-0.4\,V$ and $-0.5\,V$ for $1\,mAh/cm^2$ and $3\,mAh/cm^2$, respectively. A peak can be seen at the beginning of every half cycle, after which the potential is reduced briefly before starting to increase. Even though these peaks appear to be similar to a typical nucleation peak, they can not necessarily be assigned to nucleation of sodium metal on the WE. Due to the high reactivity of sodium metal, a native layer of reaction products quickly forms on the surface of the sodium metal, despite being handled inside an Ar-filled glovebox [29]. Trace amounts of other elements present in the glovebox are enough to form a surface layer, typically very resistive. The surface layer results in a larger potential needed initially to strip sodium from the CE until fresh sodium is exposed underneath the layer, reducing the overpotential needed for further stripping [29]. The stripping process at the CE can thus also contribute to the peak, making it difficult to determine whether or not sodium is actually being plated on the WE just based on the peak.

In addition to the initial peak, Figure 5.1 also shows the rapid polarization during subsequent cycling. Initially for each half cycle, the potential increase is approximately linear. However, for the 3 mAh/cm^2 cell the potential starts to increase more rapidly after about 2 h, almost reaching the −2 V cut-off during the first deposition. When the current is reversed, the peak height is increased compared to the previous half cycle, a trend that is more pronounced for the longer cycles as seen in the almost 1 V peak for the 3 mAh/cm^2 cell at $t = 3$ h compared with the 1 mAh/cm^2 cell. Depending on which processes are causing the peaks, these results could be interpreted slightly differently. As discussed above, the peak could have contribution from either sodium plating on the WE, sodium stripping from the CE, or both. However, disentangling the different possible processes from GCPL data alone is difficult in this case, as that would require a three-electrode cell to monitor the WE and CE potentials separately. As we are limited to a two-electrode setup here, additional characterization is required to gain further insight into what is happening during cycling.

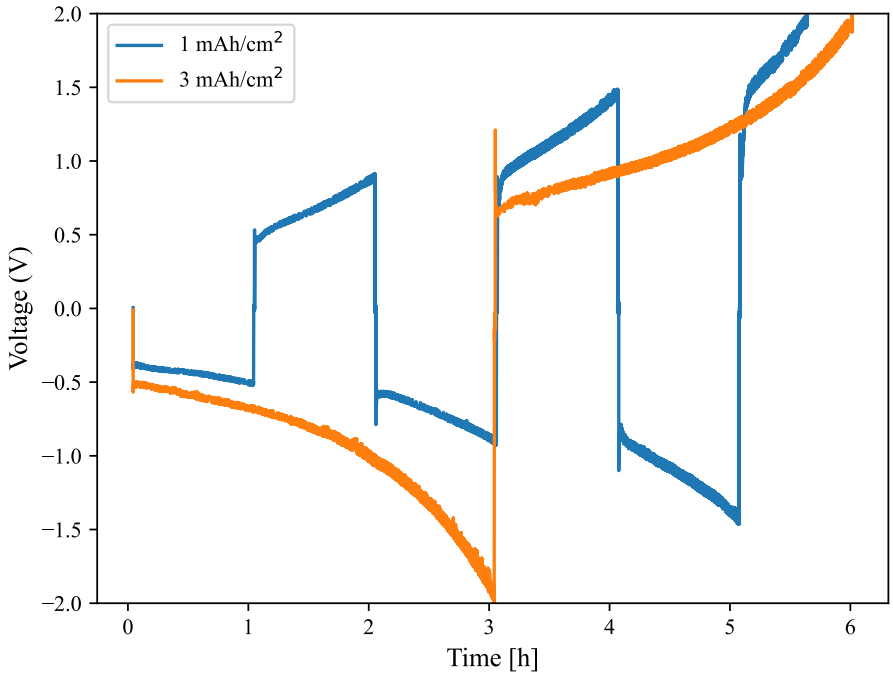

Figure 5.1: Galvanostatic cycling of symmetric Na/NPS/Na cells. The cells were cycled at 1 mA/cm^2 with areal capacities of 1 mAh/cm^2 and 3 mAh/cm^2.

Although the two curves in Figure 5.1 exhibit slightly different characteristics, they surprisingly polarize to 2 V approximately simultaneously. With potentials this large, it is not certain that sodium is being plated at all. Rather, it could be the case that the cycling of the cell is simply driving (electro)chemical reactions back and forth without any sodium being plated, since electrode potentials may be outside of the narrow electrochemical stability window of NPS [58]. The GCPL

data could in that case give the illusion of sodium being plated on the WE, but instead the sodium stripped from the CE would simply be consumed continuously in side reactions without being deposited on the WE. This could also be due to poor ionic conductivity in the system, either in the bulk electrolyte, at the interphase, or both. A moderately high current of 1 mA/cm^2 could in that case result in a large Ohmic overpotential. To analyse these questions further, additional electrochemical characterization is required.

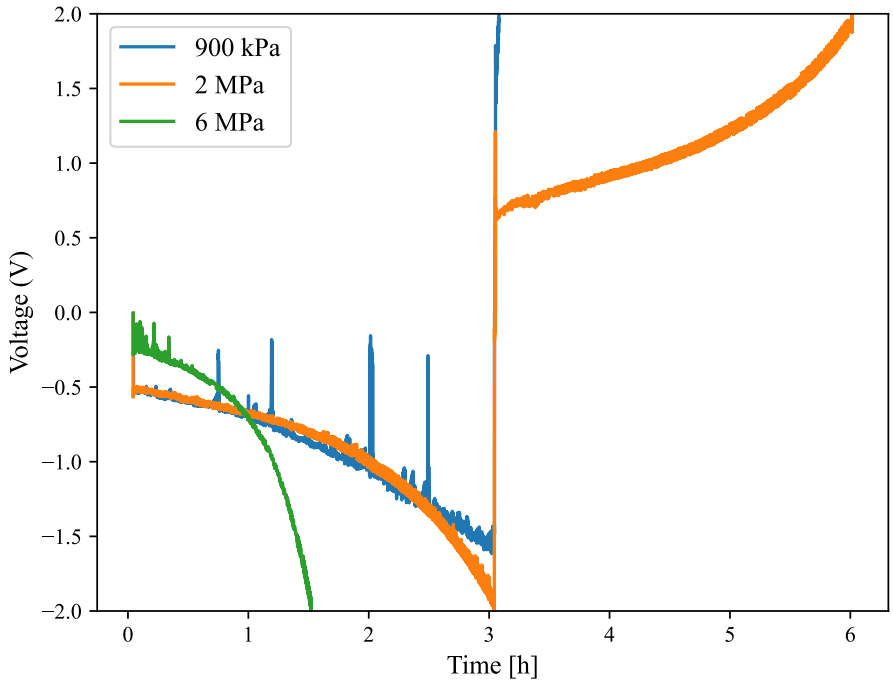

Figure 5.2: Galvanostatic cycling of symmetric Na/NPS/Na cells, comparing different stack pressures. The cells were cycled at 1 mA/cm^2 with an areal capcity of 3 mAh/cm^2.

GCPL was also performed on symmetric cells where the stack pressure was varied to investigate whether the polarization could be a result of bad interfacial contact, see Figure 5.2. Similar characteristics can be seen for the different pressures, however 2 MPa appears to cycle the best, at least completing one full cycle before polarizing to 2 V. The 900 kPa cell seems to polarize slightly slower during the first half cycle, although it immediately fails to strip. Contact loss at solid-solid interfaces is a known issue in SSBs which might explain the immediate polarization during stripping, if 900 kPa stack pressure is too low to ensure good physical contact at the interface [59]. 6 MPa appears to have noticeable influence on the polarization rate, as -2 V is reached within only 1.5 h of deposition. If the large overpotential is a result of poor interfacial contact, a higher stack pressure should improve the electrochemcial performance. However, when comparing the three stack pressures in Figure 5.2, the opposite trend can be seen where increased stack pressure tends to cause more

rapid polarization. Rather than poor interfacial contact, this trend suggests that the polarization mechanism is instead connected to (electro)chemical degradation between sodium metal and NPS. A higher stack pressure could push the soft sodium metal further into the electrolyte as well as enlarge the electrode diameter, increasing the contact area and subsequently the reaction rates between the two materials. As the yield strength of sodium is only 0.2-0.3 MPa, creep of sodium metal at stack pressures this high is very likely, making the above scenario a possible explanation of the trend of increased polarization rate for higher stack pressure.

5.1.2 Deposition in Asymmetric Cells

To further investigate which processes are occurring in this system, in particular whether or not we are actually plating sodium metal, an asymmetric cell with sodium metal as CE was tested by depositing $1\,\mathrm{mA/cm^2}$ until failure, see Figure 5.3. The initial stages of deposition show an initial overpotential peak, followed by a brief stabilization around $-200\,\mathrm{mV}$ until a sudden potential step occurs at $t = 0.06\,\mathrm{h}$. The initial peak is a typical sign of sodium plating on the CC, and the plateau that follows would then be the subsequent growth of formed nuclei [4]. However, there is also the possibility that the peak is not necessarily due to the plating itself, rather from the energy barrier of stripping through the surface layer on the CE, as discussed before. The potential step likely indicates a soft short circuit since the potential does not fully reach 0 V, which would indicate a hard short circuit. This could be due to filament growth from the freshly deposited sodium, creating a low-resistance path through the electrolyte. Although, at this point only $0.06\,\mathrm{mAh/cm^2}$ is plated, corresponding to a $0.5\,\mu\mathrm{m}$ layer of sodium metal (if plated homogeneously), which is such a small amount that dendrite growth seems unlikely. Rather, it could be due to sodium creep through cracks in the electrolyte. After the suspected short circuit the cell voltage becomes significantly more unstable, a phenomenon that increases along with the subsequent polarization. Surprisingly, the cell still polarizes after 1 h in spite of the short circuit, which points towards some reaction that degrades the low-resistance pathway.

As mentioned, poor ionic conductivity could be an explanation to the high overpotentials seen in the cycling data presented. In order to investigate this, another asymmetric Al/NPS/Na cell was tested through galvanostatic deposition at a lower current density. The comparison between the two cells is presented in Figure 5.4. By studying the deposition onset of the two cells, a reduction in overpotential is seen, which is expected as the current density is lower as per the (not necessarily linear) relation between current and polarization, mentioned in Section 2.1. The $0.1\,\mathrm{mA/cm^2}$ cell then proceeds to deposit in a stable manner, before severe polarization occurs once again after 1 h. Since the polarization effect is observed for both current densities at approximately the same time, ionic conductivity is likely not the main reason for the high overpotential.

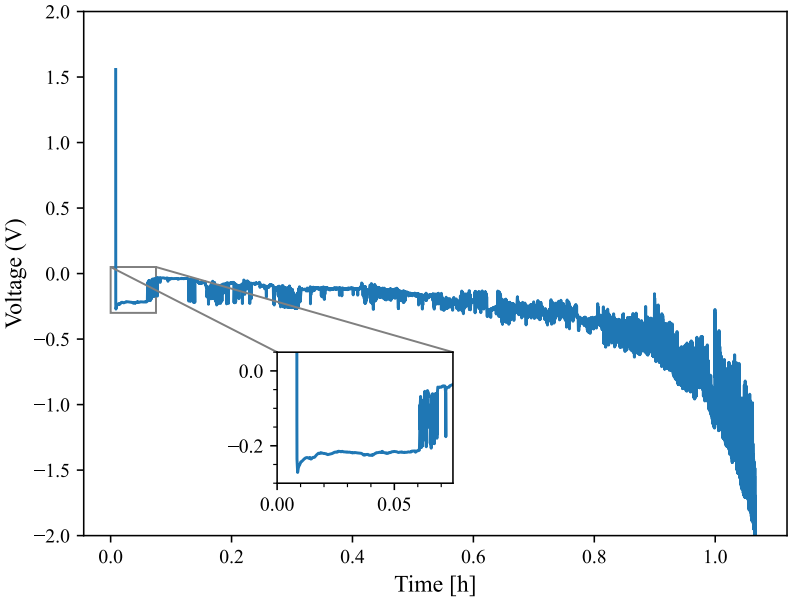

Figure 5.3: Deposition until failure in asymmetric Al/NPS/Na cell. The cell was deposited with a current density of $1\,\mathrm{mA/cm^2}$.

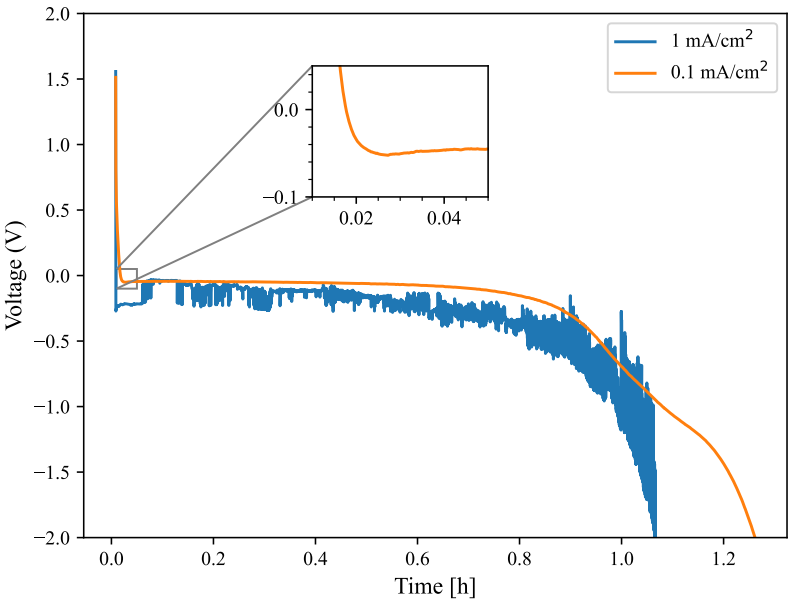

Figure 5.4: Deposition of sodium until failure in two asymmetric Al/NPS/Na cells, cycled at $1\,\mathrm{mA/cm^2}$ and $0.1\,\mathrm{mA/cm^2}$, respectively.

.

5.1.3 Comparison of Cycling Performance with Lithium-Based Cells

To give context to the rather extreme electrochemical behaviour of the sodium cells, 1 mAh/cm^2 GCPL was performed also on a similar Li-based symmetric cell, as seen in Figure 5.5. The symmetric Li/LPSC/Li exhibits a significantly more stable cycling behaviour, with a smaller overpotential indicating less pronounced polarization effects. Starting at 25 mV, the overpotential then increases to 40 mV after ten full cycles. In addition to the reduced tendency for polarization, one can also note the lack of a clear peak at the start of each half cycle for the lithium cell. While there is a peak visible at the start of every half cell in Na/NPS/Na cells, both long and short cycling, there seems to be none at any point for Li/LPSC/Li. Recalling the discussion on how a resistive interphase at the stripped electrode could give rise to an initial peak, it appears that effects from such processes are noticeably reduced in the case of the symmetric lithium cell.

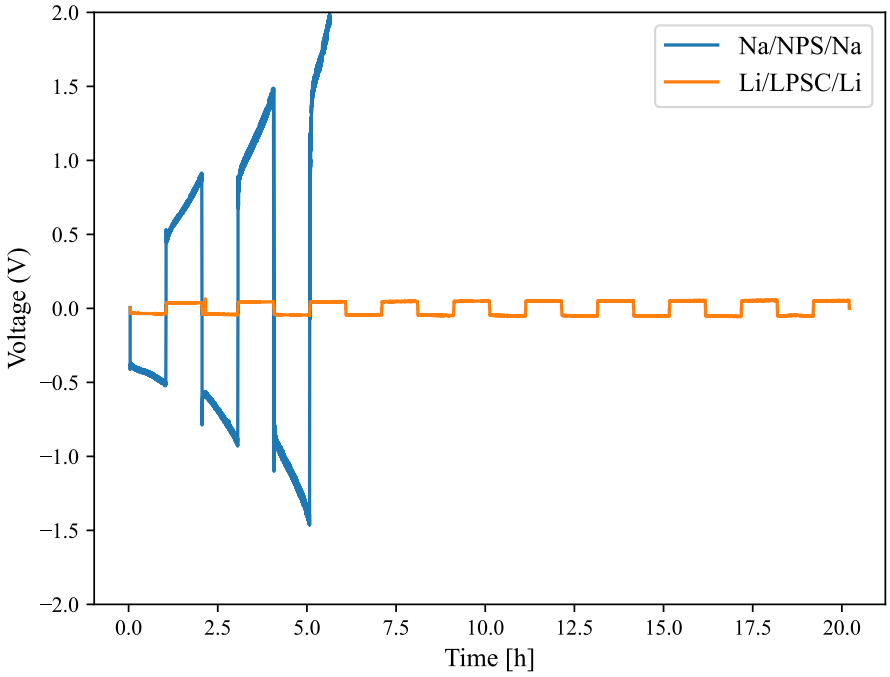

Figure 5.5: GCPL comparison between symmetric Na/NPS/Na and Li/LPSC/Li cells, cycled at 1 mA/cm^2

5.2 Degradation Mechanisms at the Sodium Metal-Electrolyte Interface

The poor cycling performance of the symmetric and asymmetric cells raises questions to what the failure mechanisms could be. In order to gain further insight into the processes at the sodium metal/electrolyte interface, EIS measurements were made

to track the impedance evolution over time. The electrochemical data is then paired with imaging using XTM.

5.2.1 Electrochemical Impedance Spectroscopy of Symmetric Cells

Impedance measurements were taken before and after one 3 mAh/cm^2 cycle at 1 mA/cm^2 for a symmetric Na/NPS/Na cell, at which point the cell voltage hit the 2 V cut-off. For comparison, EIS was also measured on a symmetric NA/NPS/Na cell that was simply resting at OCV for 6 h. The results are shown in Figure 5.6. The characteristics of the impedance spectra is rather similar for the two cells, where there is a single semicircle that dominates the spectrum already for the pristine cell. The diameter of the pristine semicircle is 500 Ω · cm^2, which increases to 1600 Ω · cm^2 after one 3 mAh/cm^2 cycle at 1 mA/cm^2. Such an impedance increase could be caused by morphological changes of the sodium metal electrodes. Inhomogeneous stripping of sodium metal can cause void formation at the electrolyte interface, resulting in poor contact with the electrolyte which in turn causes current constriction at the remaining contact points, manifesting as increased cell impedance. Another possible process that could account for the impedance evolution is the formation of an interphase with poor ionic conductivity. Considering instead the cell that rested at OCV for 6 h, it is clear that the same impedance evolution occurs even without any cycling at all. This suggests that some purely chemical degradation occurs upon contact between sodium metal and NPS, causing the severe polarization seen in the symmetric and asymmetric cells with sodium metal electrodes in Figure 5.1 and 5.4.

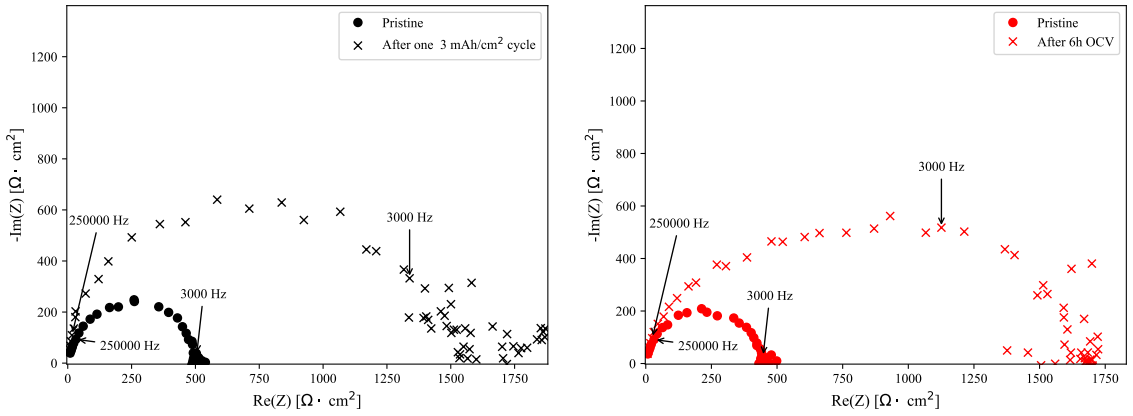

(a) **(b)**

Figure 5.6: EIS of symmetric Na/NPS/Na cells, comparing the impedance evolution after a) one full 3 mAh/cm^2 cycle and b) OCV for 6 h.

The impedance spectra are rather noisy, especially at lower frequencies. Thus, the large semicircle discussed above is the only feature clearly visible in the spectra, making any equivalent circuit fitting difficult in this case. However, some additional

information about the process connected to the large semicircle may be extracted by studying the frequency range at which the semicircle occurs. As indicated by the frequency marking in Figure 5.6 this range is quite wide, spanning 100 kHz to 1 kHz. This covers large parts of typical high and mid frequency spectra, making the assignment of individual processes difficult simply based on the frequency range. The large semicircle may be the result of a single process, but there is also the possibility that several different mechanisms are hidden within this range.

5.2.2 XTM Imaging of Sodium Metal-Electrolyte Interface

The impedance evolution seen in the results from EIS measurements suggests a rapid chemical degradation at the interface between sodium metal electrodes and NPS. To better understand the interface process(s) that cause this impedance evolution, *in situ* nanoCT was used to image a symmetric Na/NPS/Na cell that has been resting at OCV. The resulting images can be seen in Figure 5.7, showing both the top and bottom electrodes at 2 h and 18 h after cell assembly. The grayscale in the images is such that darker areas correspond to more attenuating materials, and vice versa. In the 2 h images 5.7c and 5.7a, three layers of distinct phases can be observed. Recalling Table 3.1, sodium is the least attenuating element out of those expected at the interface region, making sodium a likely candidate for the topmost and bottommost layers in Figures 5.7a and 5.7c, respectively. As NPS is the most attenuating, it is reasonable to assign the large darker areas to the electrolyte. Interestingly, a third intermediate phase can be clearly distinguished, with attenuation somewhere in between that of sodium and NPS. This might suggest that the intermediate layer contains a mixture of sodium and NPS, which points towards the some kind of reaction. As shown in previous works, the degradation products Na_2S and Na_3P both have been found at the sodium metal/NPS interface [22].

Looking instead at Figures 5.7d and 5.7b, showing the evolution after some additional 16 h OCV, a significant difference can be seen. At both the top and bottom electrodes it seems that the intermediate phase has grown, while the lighter phase appears to almost have disappeared from the field of view. Some lighter spots can still be seen at the very edge of the image, hinting that the sodium layer may be located just outside of the field of view. This evolution would indicate that the interphase has grown into the sodium metal, with approximately 5 µm to 20 µm difference in thickness between the two time stamps imaged here. However, it is worth noting that already after 2 h the intermediate layer is rather thick at about 25 µm to 40 µm. The growth rate seems to slow down slightly, meanwhile the impedance growth continues linearly or even slightly accelerating, judging from Figure 5.7e. Thus it seems to be something else than simply the growth depth into the fresh sodium that affects the impedance of the cell.

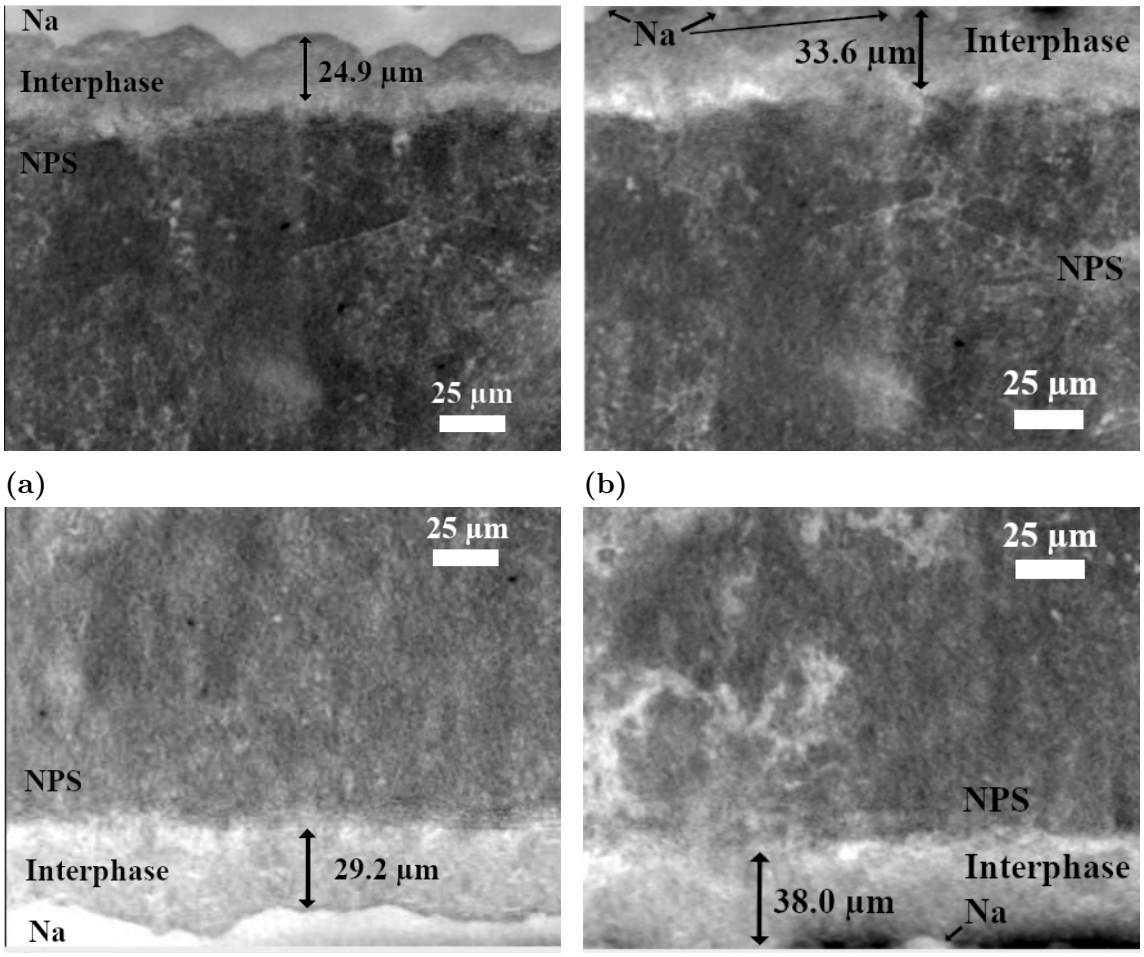

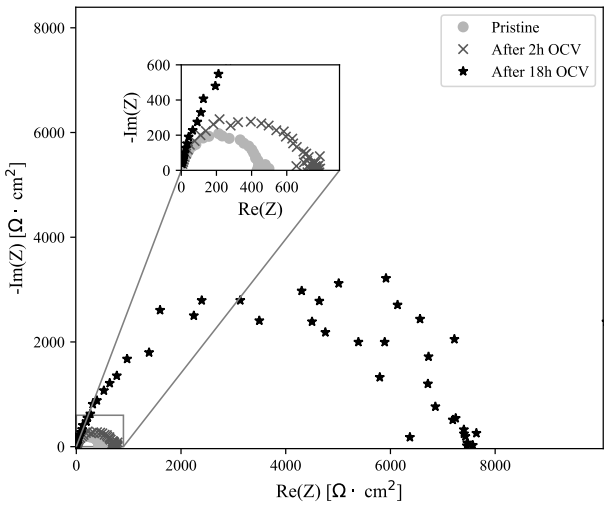

(e)

Figure 5.7: Nano-FT images of symmetric Na/NPS/Na cell that has been aged at OCV. Top electrode after a) 2h and b) 18h. Bottom electrode after c) 2h and d) 18h Corresponding EIS measurements after 2h and 18h OCV, as well as the pristine EIS for reference [60].

An image with higher resolution of the bottom electrode is presented in Figure 5.8. Some similarities can be seen with the 250 nm images discussed previously, such as the three areas of different intensity speculated to be sodium, interphase and electrolyte. With the higher resolution, some morphological details become visible that were previously not seen. The intermediate layer seems not to be entirely homogenous, as lamella-like brighter areas are dispersed throughout the interphase. There could be multiple explanations to what this could be. One possible explanation is that the two phases seen in the intermediate layer correspond to the two reaction products Na_2S and Na_3P, as their attenuation coefficients vary slightly (see Table 3.1). In that case, there seems to be some inhomogeneity in how the two compounds are distributed within the interphase, reminiscent of phase separation by spinodal decomposition [61]. Another possibility is the brighter spots correspond to sodium metal which is yet to react, since the brightness seem to correspond well with that of sodium, seen in the lower right corner of the image. The degradation between sodium and NPS does in that case not occur homogeneously at the 1 µm scale, as small pockets of sodium seem to remain for longer. It has been reported that while Na_2S is electronically insulating, Na_3P has a rather narrow bandgap which could increase the electronic conductivity of the mixture [62]. If the electronic conductivity is high enough, the present interphase could be classified as MCI type. The mixed ionic and electronic conductivity would explain the rapid and continuous interphase growth through chemical degradation reactions between sodium metal and NPS.

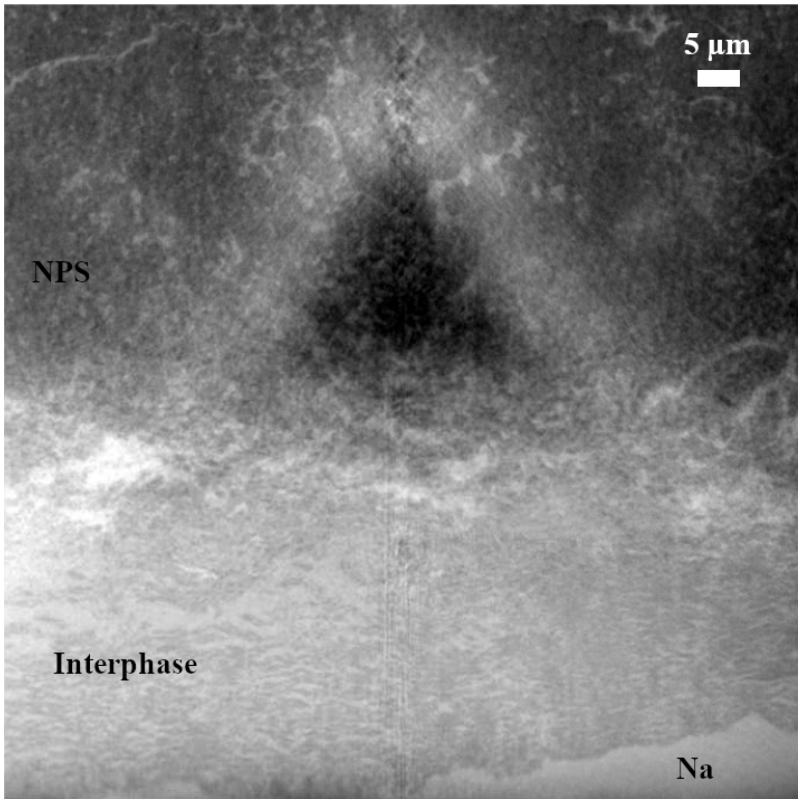

Figure 5.8: Nano-HT (50 nm resolution) image of the sodium metal/electrolyte interface at the bottom electrode [60].

5.3 Sodium-Tin Alloy as Counter Electrode

Due to the severe degradation occurring between NPS and sodium metal discussed in the previous sections, it is difficult to gain insights into the mechanisms of sodium metal deposition in cell configurations containing sodium metal electrodes, as the electrochemical data is likely to be overshadowed by degradation at the CE. It has been suggested that Na-Sn alloys could exhibit improved stability against NPS [32]. Therefore, Na_3Sn was introduced as CE to replace pure sodium metal in asymmetric cells in efforts to mitigate degradation mechanisms at the CE and highlight processes at the WE.

5.3.1 Galvanostatic Cycling of Asymmetric Cells with Sodium-Tin Alloy as Counter Electrode

Figure 5.9 shows a full 1.3 mAh/cm^2 cycle of an asymmetric cell using the Na_3Sn alloy as CE. A noticeable difference is seen in the deposition behaviour when comparing with the corresponding measurement with sodium metal as CE, as discussed in section 5.1.1. While the cell using sodium metal as CE polarizes quickly after only 1 h, the Na_3Sn CE seems to somewhat stabilize the system, showing no apparent polarization increase within 3 h of deposition. This difference in polarization is likely due to the improved stability of Na_3Sn against NPS compared with sodium metal. Using this setup, an attempt was made strip the plated sodium after deposition. However, as seen in Figure 5.9 this was barely possible since the cell polarized after only a minute of stripping, yielding $< 1\,\%$ Coulombic efficiency.

The reason for this poor electrochemical performance could be that the plated sodium metal is either consumed completely before the stripping begins, or that the plated sodium is covered in a very resistive interphase that is difficult to strip through. An additional third explanation might be that there is no plating of sodium at all, so there is no sodium metal on the Al current collector at any point during the deposition process. Nevertheless, there are indications of sodium plating in Figure 5.9, in particular the initial overpotential peak and the 0 V vs Na^+/Na during the 30 s OCV resting in between the plating and stripping.

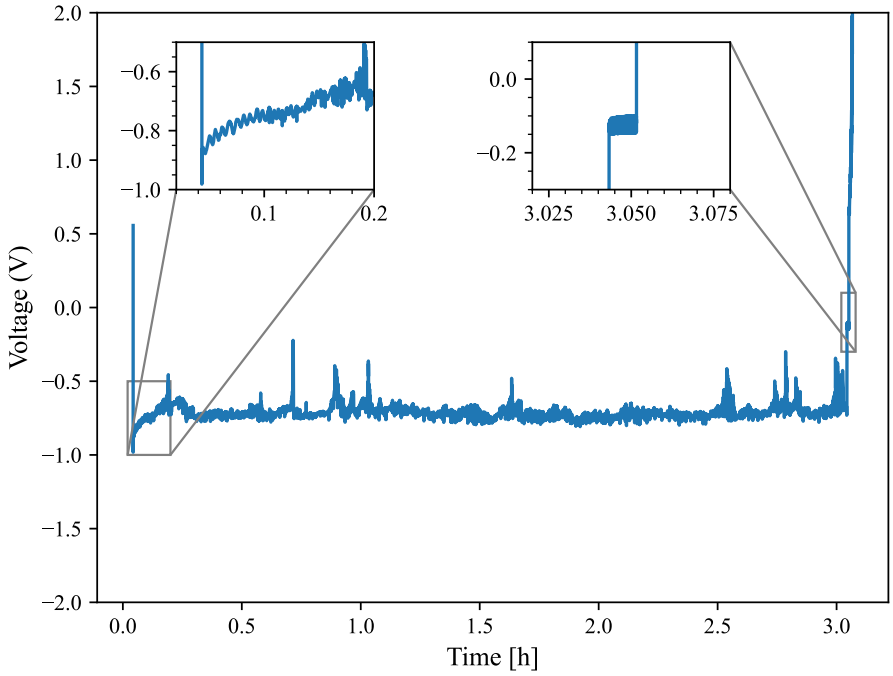

Figure 5.9: GCPL of asymmetric Al/NPS/Na_3Sn cell at 0.44 mA/cm^2. After the 3 h deposition half cycle, the stripping lasted only for about 1 min before cut-off was reached.

5.3.2 Coulometric Titration Time Analysis

A modified variant of CTTA was performed on asymmetric Al/NPS/Na_3Sn cells to quantitatively characterize the degradation of plated sodium. Figure 5.10 shows the electrochemical results from this measurement, where 0.44 mAh/cm^2 is deposited onto the Al substrate, followed by monitoring of the subsequent OCV evolution. Immediately after the deposition ends, the OCV was −130 mV, rising quickly to about −100 mV where the potential stabilizes somewhat. However, the potential continues to increase steadily, approaching 1 V after 2.4 h of OCV. After $t = 3$ h the OCV starts to plateau again at around 1 V, which could indicate near full consumption of the deposited sodium.

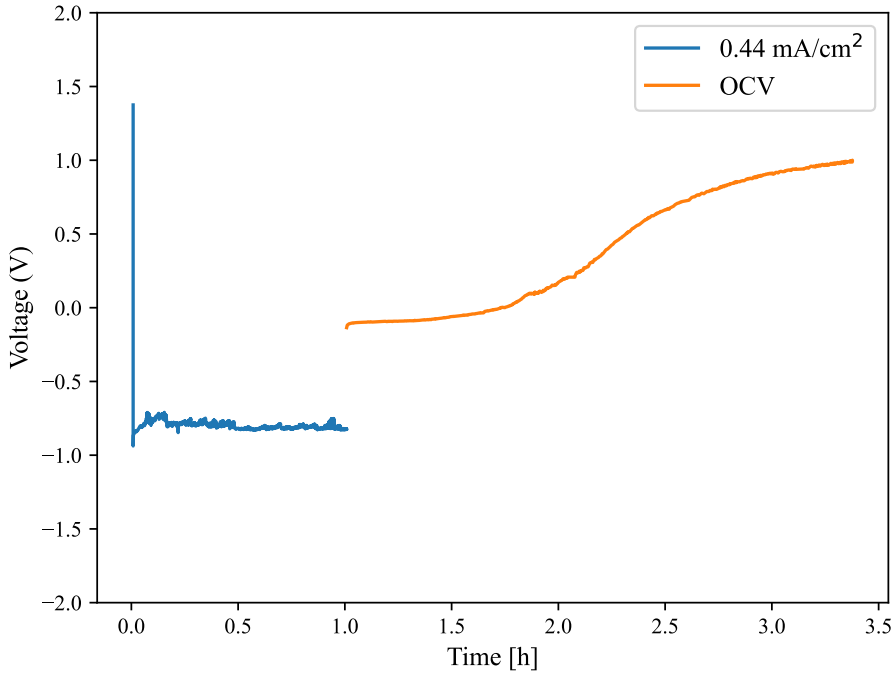

Figure 5.10: Coulometric titration time anaylsis on an asymmetric Al/NPS/Na_3Sn cell. 0.44 mAh/cm^2 was deposited onto the Al CC.

A similar experiment was performed with *in situ* XTM to image the evolution at the Al CC during plating and OCV. Figure 5.11 shows the interface between NPS and the Al CC, imaged before and after 2.33 mAh/cm^2 deposition. No clear layer of deposited sodium can be seen just by visual inspection of the images 5.11a and 5.11b, contradicting the electrochemical results in Figures 5.9 and 5.10 that suggest that some amount of sodium is plated on the CC. An estimated 20.6 µm of dense sodium would be expected after 2.33 mAh/cm^2 if plated homogenously, using Equation 3.4, which should be clearly visible in this resolution. However, the high rate of sodium consumption shown in Figure 5.10 could explain why no sodium is visible, as a majority of the plated sodium could be continuously consumed in side reactions during the deposition. Additional image analysis is required in order to study the interface evolution, which was not possible within the scope of this project. Since the nano-FT images do not capture the entire cell within the field of view, there is also the possibility of sodium plating somewhere outside of the field of view, closer to the edge of the cell.

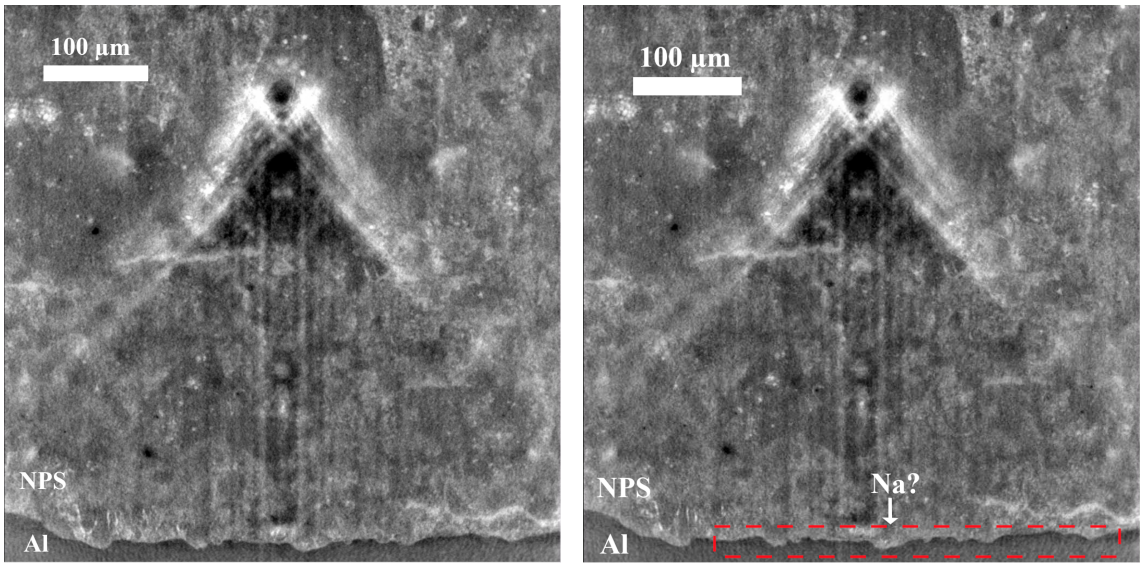

(a) **(b)**

Figure 5.11: *In situ* nano-FT images of an asymmetric Al/NPS/Na_3Sn cell, taken at the WE (bottom electrode). a) Pristine scan of the cell before cycling. b) In-situ image after 2.33 mAh/cm^2 deposition [60].

5.3.3 XTM Imaging of Sodium-Tin Alloy-Electrolyte Interface

Nano-FT images were taken at the CE, in order to study the evolution at the interface between Na_3Sn alloy and NPS, presented in Figure 5.12. Figure 5.12a displays the full field of view, in which a majority of the image is comprised of the NPS (gray area) , and a layer of the highly attenuating Na_3Sn is visible at the top. By comparing 5.12b and 5.12c, no clear differences can be spotted. This presents a drastically different situation for the NPS/Na_3Sn interface compared with NPS/Na, indicating a significantly increased stability. Taking into account that the cell was assembled 12 h before the images in Figures 5.12b and 5.12c were taken, and that the images are taken 3 h 20 min apart, further highlights the stabilizing effect of the tin alloy.

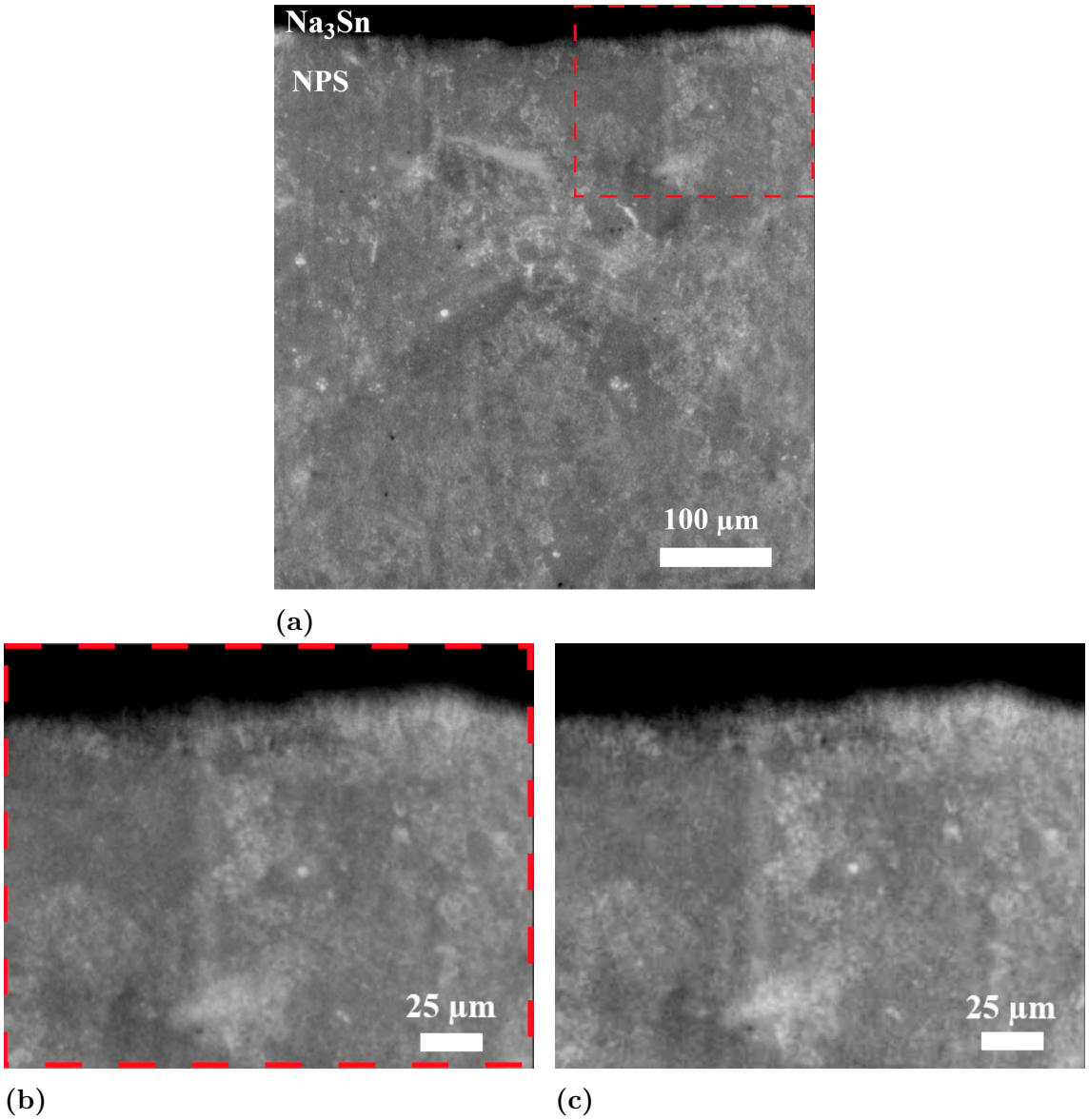

Figure 5.12: *In situ* nano-FT images of an asymmetric Al/NPS/Na_3Sn cell, taken at the CE (top electrode) for a) pristine cell with full field of view, b) pristine cell zoomed in at the top right corner and c) zoomed in on the same area after 2.33 h of 1 mA/cm^2 deposition followed by 1 h OCV [60].

5.4 Chemo-mechanical failure mechanisms

As mentioned in section 2.4, NaSSBs are prone to electro-chemo-mechanically linked mechanisms that may impact cell performance, or even cause immediate cell failure if severe enough. This section will present some mechanical phenomena observed throughout this project, and discuss their connection to the (electro)chemical processes previously discussed in this chapter.

5.4.1 Crack Formation due to Interfacial Effects

Figure 5.13 displays full field of view nano-FT images of the same cell discussed in section 5.2.2, however now we shift focus from the interphase growth to the evolution of the electrolyte. In the 2 h-aged cell in Figure 5.13a, some low attenuating stripes are visible throughout the electrolyte, which are most likely cracks in the electrolyte pellet. The larger vertical crack to the right can be seen reaching down to make contact with the top of the interphase, but does not continue down into the interphase. This might suggest that the crack had formed already in the pristine state, before contact was made between the sodium metal electrode and the NPS pellet. An alternative explanation would be that the interphase is more ductile and less susceptible to fracture than NPS. Thus, if the crack formed later during the OCV resting, the mechanical stress causing the fracture would be relieve more effectively in the interphase, preventing the interphase to crack as well. It was seen in Figure 5.8 that the interphase possibly contains regions of sodium metal that is yet to react. Since sodium is very soft and deformable, it could help reduce the risk of fracture in the interphase. Earlier works that investigated interphase properties in relation to stack pressure seem to confirm that the interphase indeed is less prone to cracking than the electrolyte itself, even providing protection against sodium dendrite growth and/or plastic flow through cracks and porosities in the NPS [63]. This might provide insights into the increased tendency for short circuiting in asymmetric cells compared with symmetric cells, seen in Figure 5.4. Since the freshly deposited sodium on the Al CC does not have a native surface layer of reaction products, in contrast to the excess sodium electrodes, there could be an increased risk of sodium growth up into any cracks in the electrolyte.

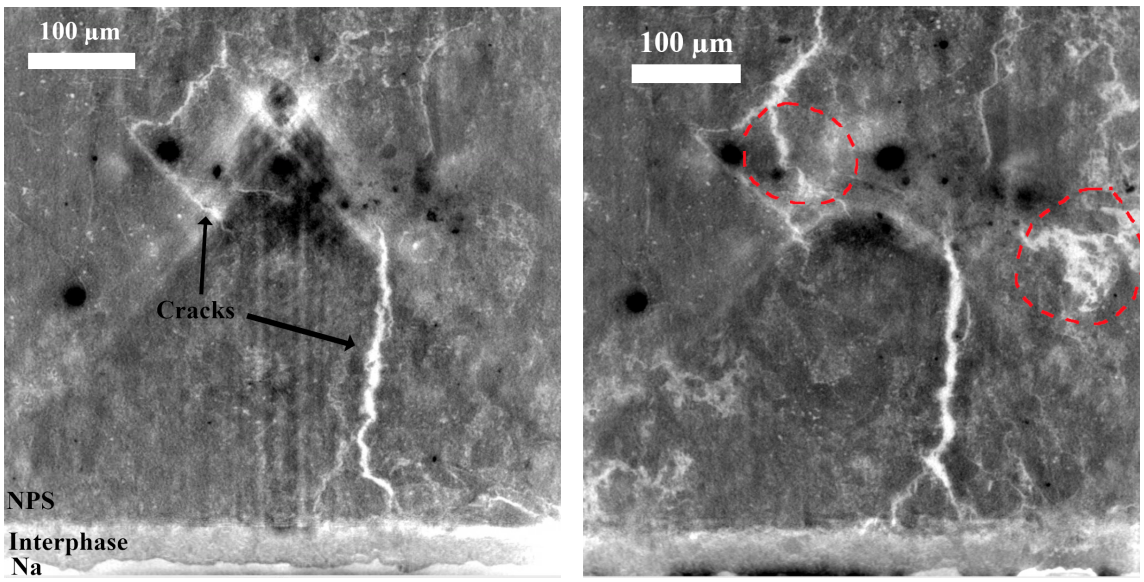

(a) **(b)**

Figure 5.13: Nano-FT images of the bottom electrode in a symmetric Na/NPS/Na cell. Both images show full field of view $527.44 \times 527.44\,\mu m^2$, after a) 2 h and b) 18 h of resting at OCV [60].

Now, comparing with the 18 h aged sample, some evolution of the cracks can be observed, primarily in the one upper left one marked in Figure 5.13b. A newly formed crack is seen growing vertically down from the original formation. Additionally, the larger vertical crack appears to have widened slightly compared with the 2 h aged sample. This evolution indicates that crack formation can occur even while the cell is resting at OCV, without any plating or stripping which is known to cause similar issues. Because the interphase growth upon contact between sodium metal and NPS appears to be rather fast, it might be so that volume changes due to interphase growth at both electrodes could provide sufficient stress/strain to ultimately fracture the electrolyte.

5.4.2 Pressure-Induced Short Circuit

Sulfide-based solid electrolytes have the benefit of fabrication through cold-pressing, i.e. at room-temperature. However, the pressure and time of pressing can have significant influence on the properties of the produced electrolyte pellet. To investigate these properties, a comparison was made between two pellet fabrication procedures. The first procedure was pressing at 310 MPa for three minutes. The second procedure was pressing at a lower 120 MPa but instead pressing for 1 h, inspired by [64]. The two cells were then imaged *ex situ* using microCT, presented in Figure 5.14. The two electrolyte pellets show noticeable difference in morphology, where the 310 MPa pellet appears to have a denser morphology with a lower degree of porosity at the micrometer scale. The 120 MPa pellet on the other hand seem to have some areas of highly densified powder, but overall the grain size tends to be smaller, in good agreement with previous studies on pressure effects [65].

The implications of the increased degree of densification as a result of higher fabrication pressure becomes apparent when comparing the interface between the sodium metal and the electrolyte at the top electrode in Figures 5.14c and 5.14d. For the lower pressure, it appears that the sodium metal has been pressed deep into the electrolyte, indicating that the mechanical integrity of the electrolyte is insufficient to withstand plastic flow of the soft sodium, making it prone to short circuit. On the contrary, the higher pressure seems to have improved on this regard, as the electrolyte manages to prevent flow of sodium into the bulk electrolyte more effectively. Nevertheless, the sodium gets pushed into the electrolyte to some extent also for the higher pressure. Thus, the resulting contact area becomes very high which likely exaggerates the chemical degradation discussed previously.

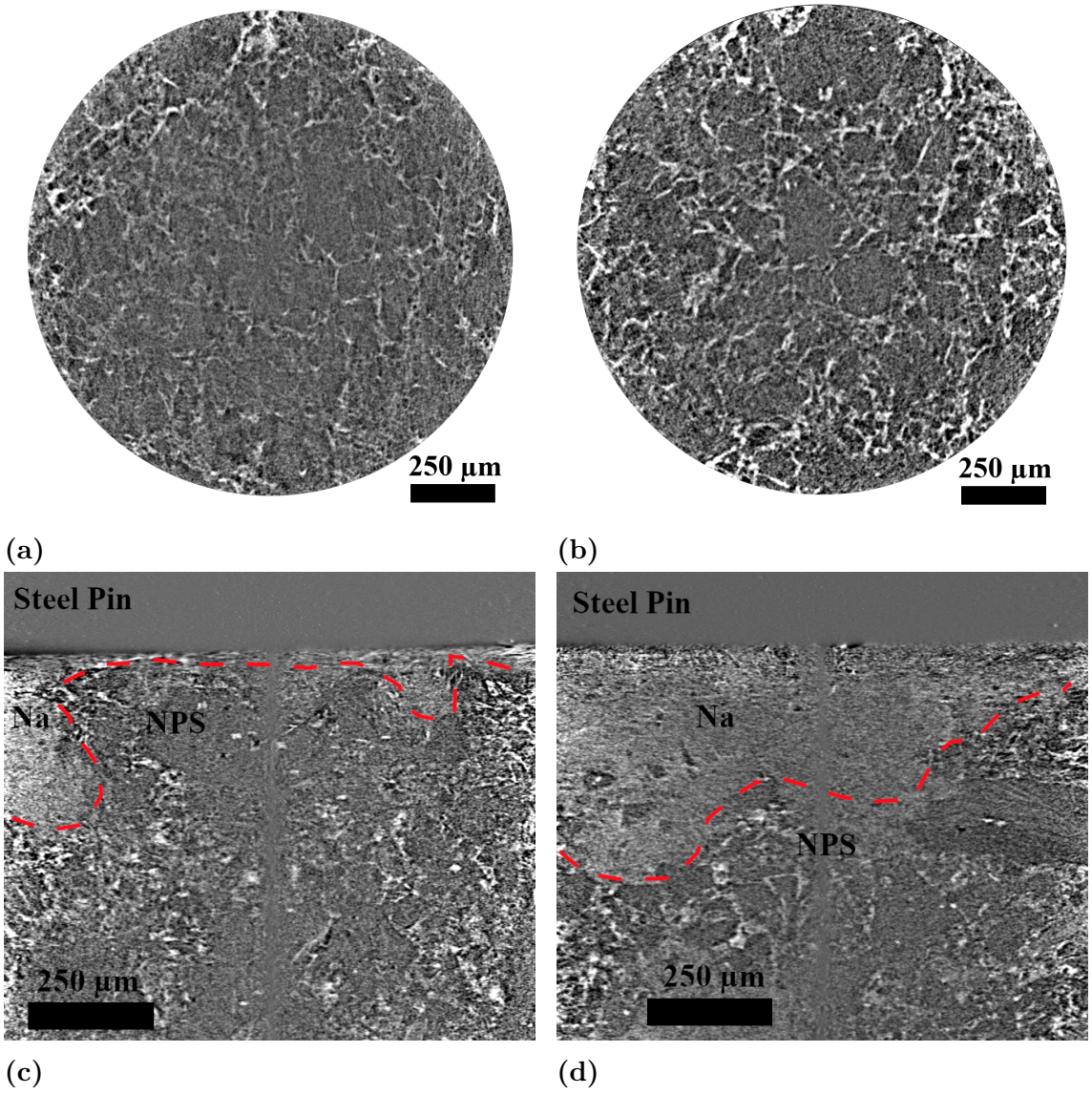

Figure 5.14: MicroCT images of horizontal cross section through the bulk of the electrolyte. The NPS pellets were cold-pressed at a) 310 MPa for 3 min and b) 120 MPa for 1 h. Subfigures c) and d) show corresponding vertical cross sections at the interface between sodium metal and NPS, where the the pellet fabrication procedure was c) 310 MPa cold-press for 3 min and d) 120 MPa cold-press for 1 h.

6
Conclusion and Outlook

In this project, the sulfide-based solid electrolyte Na_3PS_4 has been studied, with focus on the interface with sodium metal anodes. Electrochemical characterization techniques and X-ray tomographic microscopy was used to study the electrochemical performance of symmetric and asymmetric cells, perform *ex situ* and *in situ* imaging of the electrode/electrolyte interface, and analysed to correlate the interfacial evolution with cell performance. The electrochemical results show a rapid polarization for both symmetric and asymmetric cells with sodium metal electrodes. Comparing EIS measurements on cycled and OCV-aged cells suggests that chemical degradation upon contact between sodium metal and the electrolyte causes a significant increase of cell impedance, which is likely due to the growth of a resistive interphase. XTM images confirmed the presence of a thick interphase layer which continues to grow even at OCV, pointing towards a mixed-conductive interphase that fails to passivate the sodium metal electrode, resulting in continuous chemical degradation.

The results in this thesis highlight the need for future research on the interface engineering of solid-state sodium batteries, in particular with respect to sodium metal anodes and anode-free cells. Several paths have been identified as possible, including doping the electrolyte with Cl, replacing the Al foil with Al pellet pressed from Al powder as current collector, and using protective interlayers. Cl-doping is an approach that has shown indications of producing a more stable interphase layer, where the additional NaCl appears to suppress the electronic conductivity of the interphase which is responsible for the continuous chemical degradation [22]. Furthermore, pelletized current collectors have been found to improve several chemo-mechanical properties at the interface with solid electrolytes, such as better interfacial contact and more even pressure distribution [66]. Finally, protective interlayers can provide (electro)chemical stabilization at the anode/electrolyte interface, as well as improving the homogeneity of the *in situ* plated metal anode in reservoir-free cells. Silver-carbon composites have shown good performance for lithium-based SSBs, so a similar approach to NaSSBs would be very interesting to investigate [67]. By investigating these paths of future work, a better anode/electrolyte interface stability could hopefully be achieved for improved electrochemical performance and longer lifetimes of sulfide-based NaSSBs.

Bibliography

[1] B. Dunn, H. Kamath, and J.-M. Tarascon, "Electrical Energy Storage for the Grid: A Battery of Choices," *Science*, vol. 334, no. 6058, pp. 928–935, Nov. 2011. DOI: 10.1126/science.1212741.

[2] J. B. Goodenough and K.-S. Park, "The Li-Ion Rechargeable Battery: A Perspective," *Journal of the American Chemical Society*, vol. 135, no. 4, pp. 1167–1176, Jan. 2013. DOI: 10.1021/ja3091438.

[3] C. Zhao *et al.*, "Solid-State Sodium Batteries," en, *Advanced Energy Materials*, vol. 8, no. 17, p. 1 703 012, 2018. DOI: 10.1002/aenm.201703012.

[4] T. Ortmann *et al.*, "Deposition of Sodium Metal at the Copper-NaSICON Interface for Reservoir-Free Solid-State Sodium Batteries," en, *Advanced Energy Materials*, vol. 14, no. 15, p. 2 302 729, 2024. DOI: 10.1002/aenm.202302729.

[5] E. A. Olivetti, G. Ceder, G. G. Gaustad, and X. Fu, "Lithium-Ion Battery Supply Chain Considerations: Analysis of Potential Bottlenecks in Critical Metals," *Joule*, vol. 1, no. 2, pp. 229–243, Oct. 2017. DOI: 10.1016/j.joule.2017.08.019.

[6] S. Chu, S. Guo, and H. Zhou, "Advanced cobalt-free cathode materials for sodium-ion batteries," en, *Chemical Society Reviews*, vol. 50, no. 23, pp. 13 189–13 235, Nov. 2021. DOI: 10.1039/D1CS00442E.

[7] G. Liu, J. Yang, J. Wu, Z. Peng, and X. Yao, "Inorganic Sodium Solid Electrolytes: Structure Design, Interface Engineering and Application," en, *Advanced Materials*, vol. 36, no. 37, p. 2 311 475, 2024. DOI: 10.1002/adma.202311475.

[8] K. W. Beard, *Linden's Handbook of Batteries, Fifth Edition*, eng, 5th edition. New York, N.Y: McGraw-Hill Education, 2019.

[9] A. J. Bard, L. R. Faulkner, and H. S. White, *Electrochemical methods: fundamentals and applications*, eng, Third edition. Hoboken, NJ, USA Chichester, West Sussex, UK: Wiley, 2022.

[10] E. C. Cengiz, J. Rizell, M. Sadd, A. Matic, and N. Mozhzhukhina, "Review—Reference Electrodes in Li-Ion and Next Generation Batteries: Correct Potential Assessment, Applications and Practices," en, *Journal of The Electrochemical Society*, vol. 168, no. 12, p. 120 539, Dec. 2021. DOI: 10.1149/1945-7111/ac429b.

[11] S. Zhao *et al.*, "Research Progress on the Solid Electrolyte of Solid-State Sodium-Ion Batteries," en, *Electrochemical Energy Reviews*, vol. 7, no. 1, p. 3, Jan. 2024. DOI: 10.1007/s41918-023-00196-4.

[12] T. Famprikis, P. Canepa, J. A. Dawson, M. S. Islam, and C. Masquelier, "Fundamentals of inorganic solid-state electrolytes for batteries," en, *Nature*

Materials, vol. 18, no. 12, pp. 1278–1291, Dec. 2019. DOI: 10.1038/s41563-019-0431-3.

[13] J.-J. Kim, K. Yoon, I. Park, and K. Kang, "Progress in the Development of Sodium-Ion Solid Electrolytes," en, *Small Methods*, vol. 1, no. 10, p. 1 700 219, 2017. DOI: 10.1002/smtd.201700219.

[14] J. Deubener *et al.*, "Updated definition of glass-ceramics," *Journal of Non-Crystalline Solids*, 12th International Symposium on Crystallization in Glasses and Liquids, vol. 501, pp. 3–10, Dec. 2018. DOI: 10.1016/j.jnoncrysol.2018.01.033.

[15] M. Jansen and U. Henseler, "Synthesis, structure determination, and ionic conductivity of sodium tetrathiophosphate," *Journal of Solid State Chemistry*, vol. 99, no. 1, pp. 110–119, Jul. 1992. DOI: 10.1016/0022-4596(92)90295-7.

[16] A. Hayashi, K. Noi, N. Tanibata, M. Nagao, and M. Tatsumisago, "High sodium ion conductivity of glass–ceramic electrolytes with cubic Na3PS4," *Journal of Power Sources*, vol. 258, pp. 420–423, Jul. 2014. DOI: 10.1016/j.jpowsour.2014.02.054.

[17] M. Nose, A. Kato, A. Sakuda, A. Hayashi, and M. Tatsumisago, "Evaluation of mechanical properties of Na2S–P2S5 sulfide glass electrolytes," en, *Journal of Materials Chemistry A*, vol. 3, no. 44, pp. 22 061–22 065, Nov. 2015. DOI: 10.1039/C5TA05590C.

[18] J. Wolfenstine, W. Go, Y. Kim, and J. Sakamoto, "Mechanical properties of NaSICON: A brief review," en, *Ionics*, vol. 29, no. 1, pp. 1–8, Jan. 2023. DOI: 10.1007/s11581-022-04820-z.

[19] V. Lacivita, Y. Wang, S.-H. Bo, and G. Ceder, "Ab initio investigation of the stability of electrolyte/electrode interfaces in all-solid-state Na batteries," en, *Journal of Materials Chemistry A*, vol. 7, no. 14, pp. 8144–8155, Apr. 2019. DOI: 10.1039/C8TA10498K.

[20] Y. Tian *et al.*, "Compatibility issues between electrodes and electrolytes in solid-state batteries," en, *Energy & Environmental Science*, vol. 10, no. 5, pp. 1150–1166, May 2017. DOI: 10.1039/C7EE00534B.

[21] S. Wenzel, T. Leichtweiss, D. A. Weber, J. Sann, W. G. Zeier, and J. Janek, "Interfacial Reactivity Benchmarking of the Sodium Ion Conductors Na3PS4 and Sodium -Alumina for Protected Sodium Metal Anodes and Sodium All-Solid-State Batteries," *ACS Applied Materials & Interfaces*, vol. 8, no. 41, pp. 28 216–28 224, Oct. 2016. DOI: 10.1021/acsami.6b10119.

[22] E. A. Wu *et al.*, "New Insights into the Interphase between the Na Metal Anode and Sulfide Solid-State Electrolytes: A Joint Experimental and Computational Study," *ACS Applied Materials & Interfaces*, vol. 10, no. 12, pp. 10 076–10 086, Mar. 2018. DOI: 10.1021/acsami.7b19037.

[23] L. Bekaert *et al.*, "Assessing the Reactivity of the Na3PS4 Solid-State Electrolyte with the Sodium Metal Negative Electrode Using Total Trajectory Analysis with Neural-Network Potential Molecular Dynamics," *The Journal of Physical Chemistry C*, vol. 127, no. 18, pp. 8503–8514, May 2023. DOI: 10.1021/acs.jpcc.3c02379.

[24] H. Wan *et al.*, "Nanoscaled Na3PS4 Solid Electrolyte for All-Solid-State FeS2/Na Batteries with Ultrahigh Initial Coulombic Efficiency of 95% and Excellent

Cyclic Performances," *ACS Applied Materials & Interfaces*, vol. 10, no. 15, pp. 12 300–12 304, Apr. 2018. DOI: 10.1021/acsami.8b01805.

[25] O. Lenchuk, P. Adelhelm, and D. Mollenhauer, "New insights into the origin of unstable sodium graphite intercalation compounds," en, *Physical Chemistry Chemical Physics*, vol. 21, no. 35, pp. 19 378–19 390, Sep. 2019. DOI: 10.1039/C9CP03453F.

[26] B. Xiao, T. Rojo, and X. Li, "Hard Carbon as Sodium-Ion Battery Anodes: Progress and Challenges," en, *ChemSusChem*, vol. 12, no. 1, pp. 133–144, 2019. DOI: 10.1002/cssc.201801879.

[27] A. Pei, G. Zheng, F. Shi, Y. Li, and Y. Cui, "Nanoscale Nucleation and Growth of Electrodeposited Lithium Metal," *Nano Letters*, vol. 17, no. 2, pp. 1132–1139, Feb. 2017. DOI: 10.1021/acs.nanolett.6b04755.

[28] B. Lee, E. Paek, D. Mitlin, and S. W. Lee, "Sodium Metal Anodes: Emerging Solutions to Dendrite Growth," *Chemical Reviews*, vol. 119, no. 8, pp. 5416–5460, Apr. 2019. DOI: 10.1021/acs.chemrev.8b00642.

[29] J. Rizell, W. Chrobak, N. Mozhzhukhina, S. Xiong, and A. Matic, "Electrochemical Signatures of Potassium Plating and Stripping," en, *Journal of The Electrochemical Society*, vol. 171, no. 2, p. 020 517, Feb. 2024. DOI: 10.1149/1945-7111/ad2593.

[30] Z. Li, J. Ding, and D. Mitlin, "Tin and Tin Compounds for Sodium Ion Battery Anodes: Phase Transformations and Performance," *Accounts of Chemical Research*, vol. 48, no. 6, pp. 1657–1665, Jun. 2015. DOI: 10.1021/acs.accounts.5b00114.

[31] W. Hume-Rothery, "The system sodium–tin," en, *Journal of the Chemical Society (Resumed)*, no. 0, pp. 947–963, Jan. 1928. DOI: 10.1039/JR9280000947.

[32] E. A. Wu *et al.*, "A stable cathode-solid electrolyte composite for high-voltage, long-cycle-life solid-state sodium-ion batteries," en, *Nature Communications*, vol. 12, no. 1, p. 1256, Feb. 2021. DOI: 10.1038/s41467-021-21488-7.

[33] F. P. McGrogan *et al.*, "Compliant Yet Brittle Mechanical Behavior of Li_2S–P_2S_5 Lithium-Ion-Conducting Solid Electrolyte," en, *Advanced Energy Materials*, vol. 7, no. 12, p. 1 602 011, Jun. 2017. DOI: 10.1002/aenm.201602011.

[34] J. A. Lewis, J. Tippens, F. J. Q. Cortes, and M. T. McDowell, "Chemo-Mechanical Challenges in Solid-State Batteries," *Trends in Chemistry*, vol. 1, no. 9, pp. 845–857, Dec. 2019. DOI: 10.1016/j.trechm.2019.06.013.

[35] J. Xiao, "How lithium dendrites form in liquid batteries," *Science*, vol. 366, no. 6464, pp. 426–427, Oct. 2019. DOI: 10.1126/science.aay8672.

[36] A. C. Lazanas and M. I. Prodromidis, "Electrochemical Impedance SpectroscopyA Tutorial," *ACS Measurement Science Au*, vol. 3, no. 3, pp. 162–193, Jun. 2023. DOI: 10.1021/acsmeasuresciau.2c00070.

[37] P. Vadhva *et al.*, "Electrochemical Impedance Spectroscopy for All-Solid-State Batteries: Theory, Methods and Future Outlook," en, *ChemElectroChem*, vol. 8, no. 11, pp. 1930–1947, 2021. DOI: 10.1002/celc.202100108.

[38] B. Aktekin, L. M. Riegger, S.-K. Otto, T. Fuchs, A. Henss, and J. Janek, "SEI growth on Lithium metal anodes in solid-state batteries quantified with coulometric titration time analysis," en, *Nature Communications*, vol. 14, no. 1, p. 6946, Oct. 2023. DOI: 10.1038/s41467-023-42512-y.

[39] *The Nobel Prize in Physiology or Medicine 1979*, en-US. [Online]. Available: https://www.nobelprize.org/prizes/medicine/1979/summary/(accessed/.

[40] J. Vijayakumar, N. M. Goudarzi, G. Eeckhaut, K. Schrijnemakers, V. Cnudde, and M. N. Boone, "Characterization of Pharmaceutical Tablets by X-ray Tomography," en, *Pharmaceuticals*, vol. 16, no. 5, p. 733, May 2023. DOI: 10.3390/ph16050733.

[41] S. C. Garcea, Y. Wang, and P. J. Withers, "X-ray computed tomography of polymer composites," *Composites Science and Technology*, vol. 156, pp. 305–319, Mar. 2018. DOI: 10.1016/j.compscitech.2017.10.023.

[42] A. Piovesan, V. Vancauwenberghe, T. Van De Looverbosch, P. Verboven, and B. Nicolaï, "X-ray computed tomography for 3D plant imaging," *Trends in Plant Science*, vol. 26, no. 11, pp. 1171–1185, Nov. 2021. DOI: 10.1016/j.tplants.2021.07.010.

[43] Philip J Withers *et al.*, "X-ray computed tomography," *Nature Reviews Methods Primers*, vol. 1 (1), no. 18, DOI: 10.1038/s43586-021-00015-4.

[44] Matthew J. Sadd, "Operando Analysis of Materials and Processes in Next Generation Batteries," Ph.D. dissertation, Chalmers University of Technology, Gothenburg, 2021.

[45] R. Schofield *et al.*, "Image reconstruction: Part 1 – understanding filtered back projection, noise and image acquisition," *Journal of Cardiovascular Computed Tomography*, vol. 14, no. 3, pp. 219–225, May 2020. DOI: 10.1016/j.jcct.2019.04.008.

[46] X. Zhang *et al.*, "Visualizing the Future: Recent Progress and Challenges on Advanced Imaging Characterization for All-Solid-State Batteries," *ACS Energy Letters*, vol. 10, no. 1, pp. 496–525, Jan. 2025. DOI: 10.1021/acsenergylett.4c02476.

[47] J. .-. Buffière, E. Maire, P. Cloetens, G. Lormand, and R. Fougères, "Characterization of internal damage in a MMCp using X-ray synchrotron phase contrast microtomography," *Acta Materialia*, vol. 47, no. 5, pp. 1613–1625, Mar. 1999. DOI: 10.1016/S1359-6454(99)00024-5.

[48] P. Cloetens *et al.*, "Holotomography: Quantitative phase tomography with micrometer resolution using hard synchrotron radiation x rays," *Applied Physics Letters*, vol. 75, no. 19, pp. 2912–2914, Nov. 1999. DOI: 10.1063/1.125225.

[49] V. Nikitin, M. Carlsson, D. Gürsoy, R. Mokso, and P. Cloetens, "X-ray nanoholotomography reconstruction with simultaneous probe retrieval," EN, *Optics Express*, vol. 32, no. 23, pp. 41 905–41 924, Nov. 2024. DOI: 10.1364/OE.537341.

[50] J. A. Lewis *et al.*, "Linking void and interphase evolution to electrochemistry in solid-state batteries using operando X-ray tomography," en, *Nature Materials*, vol. 20, no. 4, pp. 503–510, Apr. 2021. DOI: 10.1038/s41563-020-00903-2.

[51] M. Sadd, S. Xiong, J. R. Bowen, F. Marone, and A. Matic, "Investigating microstructure evolution of lithium metal during plating and stripping via operando X-ray tomographic microscopy," en, *Nature Communications*, vol. 14, no. 1, p. 854, Feb. 2023. DOI: 10.1038/s41467-023-36568-z.

[52] J. A. Lewis *et al.*, "Accelerated Short Circuiting in Anode-Free Solid-State Batteries Driven by Local Lithium Depletion," en, *Advanced Energy Materials*, vol. 13, no. 12, p. 2 204 186, Mar. 2023. DOI: 10.1002/aenm.202204186.

[53] K. Nygård *et al.*, "ForMAX – a beamline for multiscale and multimodal structural characterization of hierarchical materials," *Journal of Synchrotron Radiation*, vol. 31, no. 2, pp. 363–377, Mar. 2024. DOI: 10.1107/S1600577524001048.

[54] G. Martínez-Criado *et al.*, "ID16B: A hard X-ray nanoprobe beamline at the ESRF for nano-analysis," *Journal of Synchrotron Radiation*, vol. 23, no. 1, pp. 344–352, Jan. 2016. DOI: 10.1107/S1600577515019839.

[55] *Periodiska Systemet - Ptable*, sv-SE. [Online]. Available: https://ptable.com/?lang=sv.

[56] S. Seltzer, *X-ray Form Factor, Attenuation and Scattering Tables, NIST Standard Reference Database 66*, en, 1995. DOI: 10.18434/T4HS32.

[57] D. Gürsoy, F. De Carlo, X. Xiao, and C. Jacobsen, "TomoPy: A framework for the analysis of synchrotron tomographic data," en, *Journal of Synchrotron Radiation*, vol. 21, no. 5, pp. 1188–1193, 2014. DOI: 10.1107/S1600577514013939.

[58] M. Mwemezi, W. B. Park, and A. B. Ikhe, "Improvement of interfacial stability between Na metal and Na3PS4 family solid electrolyte for all-solid-state sodium metal batteries," *Electrochimica Acta*, vol. 480, p. 143 919, Mar. 2024. DOI: 10.1016/j.electacta.2024.143919.

[59] J. Janek and W. G. Zeier, "Challenges in speeding up solid-state battery development," en, *Nature Energy*, vol. 8, no. 3, pp. 230–240, Feb. 2023. DOI: 10.1038/s41560-023-01208-9.

[60] M. Afiandika *et al.*, *The European Battery Hub*, en, 2028. DOI: 10.15151/ESRF-ES-2013310927.

[61] "Diffusional Phase Transformations in the Solid State," en, in *Physical Metallurgy*, Elsevier, 2014, pp. 851–1020. DOI: 10.1016/b978-0-444-53770-6.00008-3.

[62] G. Abellán *et al.*, "Exploring the Formation of Black Phosphorus Intercalation Compounds with Alkali Metals," en, *Angewandte Chemie International Edition*, vol. 56, no. 48, pp. 15 267–15 273, Nov. 2017. DOI: 10.1002/anie.201707462.

[63] C. Hänsel, P. V. Kumar, and D. Kundu, "Stack Pressure Effect in Li_3 PS_4 and Na_3 PS_4 Based Alkali Metal Solid-State Cells: The Dramatic Implication of Interlayer Growth," en, *Chemistry of Materials*, vol. 32, no. 24, pp. 10 501–10 510, Dec. 2020. DOI: 10.1021/acs.chemmater.0c03444.

[64] H. Guo, M. Häfner, H. Grüninger, and M. Bianchini, *Structure and Ionic Conductivity of Halide Solid Electrolytes based on NaAlCl4 and Na2ZnCl4*, en, Jan. 2025. DOI: 10.26434/chemrxiv-2025-01596.

[65] J.-M. Doux *et al.*, "Pressure effects on sulfide electrolytes for all solid-state batteries," en, *Journal of Materials Chemistry A*, vol. 8, no. 10, pp. 5049–5055, Mar. 2020. DOI: 10.1039/C9TA12889A.

[66] G. Deysher *et al.*, "Design principles for enabling an anode-free sodium all-solid-state battery," en, *Nature Energy*, Jul. 2024. DOI: 10.1038/s41560-024-01569-9.

[67] Y.-G. Lee *et al.*, "High-energy long-cycling all-solid-state lithium metal batteries enabled by silver–carbon composite anodes," en, *Nature Energy*, vol. 5, no. 4, pp. 299–308, Mar. 2020. DOI: 10.1038/s41560-020-0575-z.

A

Material synthesis and characterization

Synthesis and characterization of Na_3PS_4 and Na_3Sn was performed by Hao Guo, PhD student in Prof. Matteo Bianchinis group at Universität Bayreuth, using the following procedure. Stoichiometric amounts of the precursors $3Na_2S+P_2S_5$ were hand ground for 30 minutes with mortar and pestle. The powder was then transferred to an ampoule and sealed under vacuum, before heating in a furnace at 500 °C for 20 h. Two batches of electrolyte were prepared, which were characterized with electrochemical impedance spectroscopy and X-ray diffraction, shown in Figures A.1 and A.2, respectively. Synthesis of Na_3Sn was done by hand grinding stoichiometric amounts of Na metal and Sn metal with mortar and pestle for 30 minutes, followed by 8 h ball milling at 300 rpm. The resulting powder had a potential of 0.144 V vs Na^+/Na. X-ray diffraction data for the synthesized Na_3Sn is shown in Figure A.3.

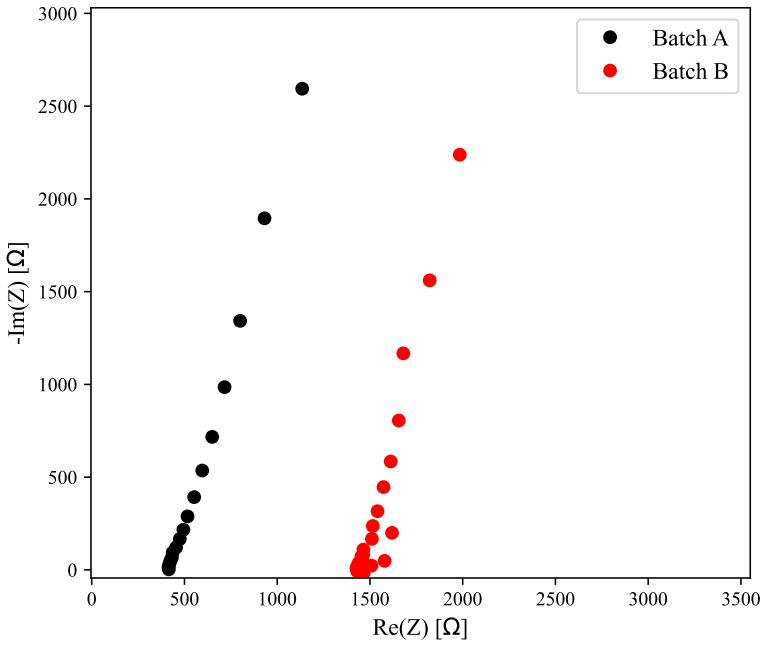

Figure A.1: Conductivity measurements of NPS with EIS for the two electrolyte batches used. Reproduced with permission from Hao Guo.

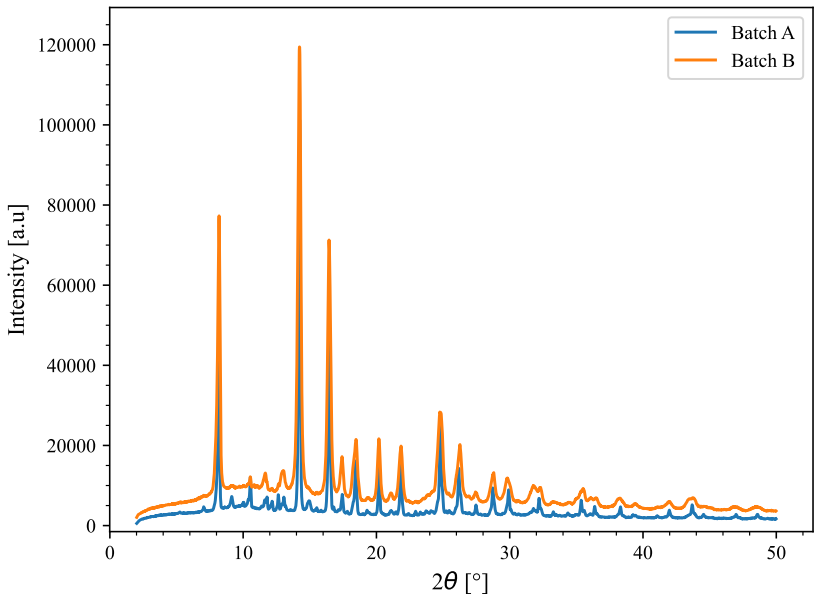

Figure A.2: X-ray diffraction data for the two batches of NPS electrolyte. Reproduced with permission from Hao Guo.

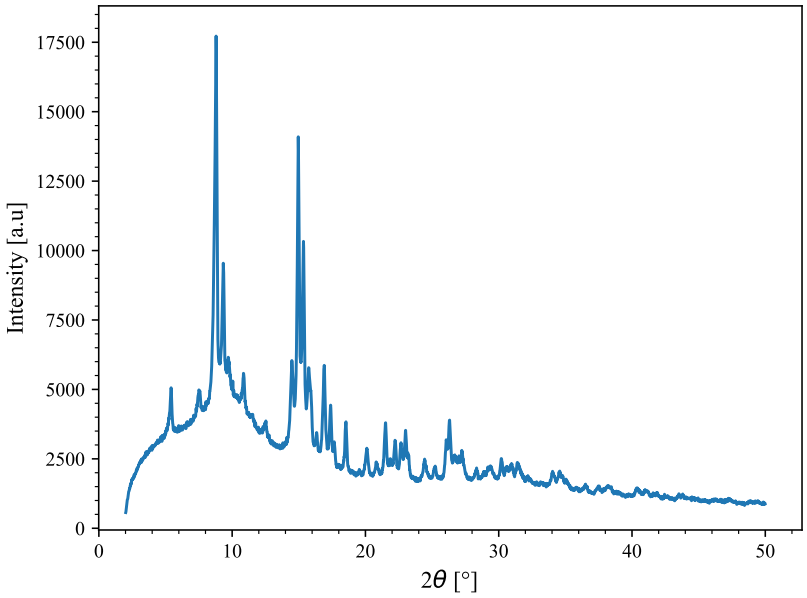

Figure A.3: X-ray diffraction data of the synthesized Na_3Sn powder. Reproduced with permission from Hao Guo.

B

Electrochemical performance of tomography cells in air

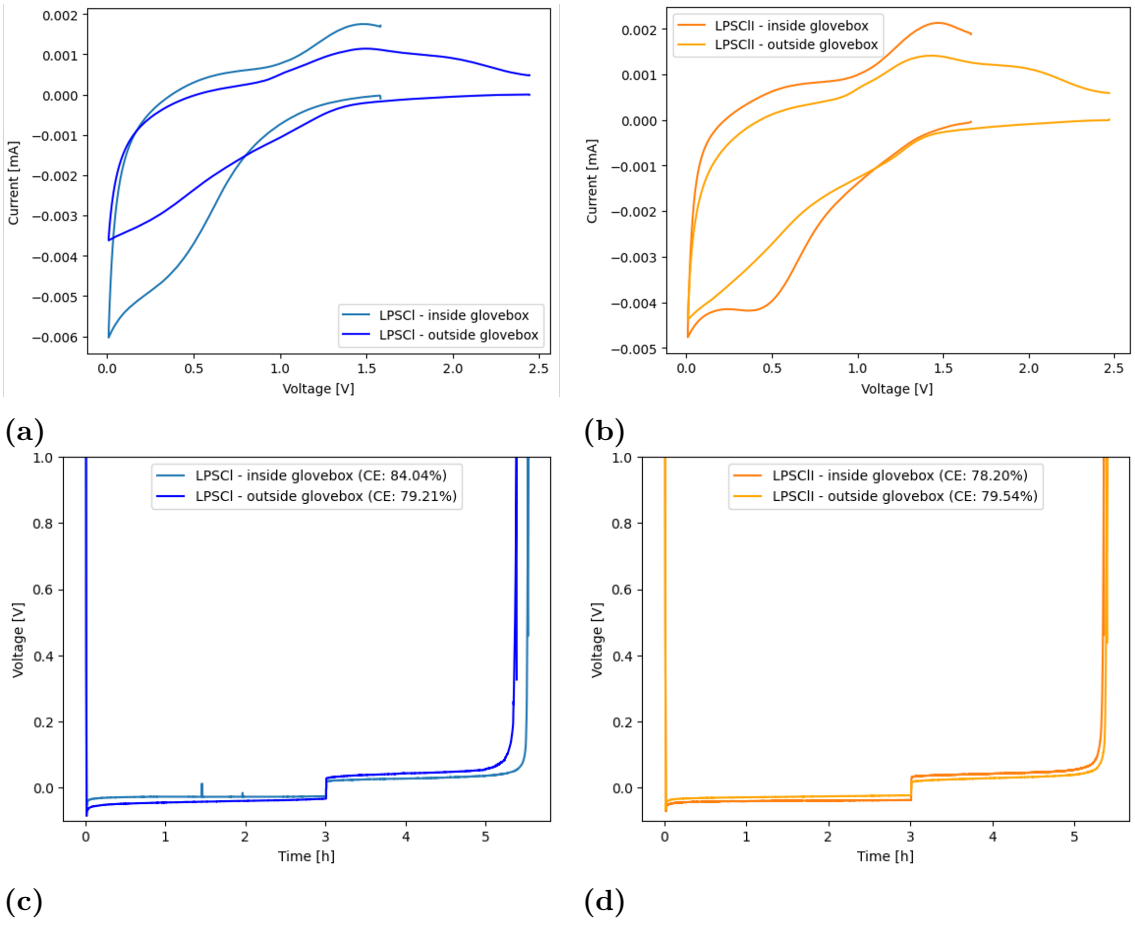

Figure B.1: Comparison of electrochemical performance of asymmetric stainless steel/electrolyte/Li cells, which have been cycled inside an Ar-filled glovebox and in air. Cyclic voltammetry with a) LPSCl and b) LPSClI electrolyte, followed by GCPL at 1 mA/cm^2 of the c) LPSCl and d) LPSClI cells, respectively. Reproduced with permission from Elin Dufvenius Esping.

DEPARTMENT OF PHYSICS
CHALMERS UNIVERSITY OF TECHNOLOGY
Gothenburg, Sweden
www.chalmers.se

CHALMERS
UNIVERSITY OF TECHNOLOGY